JOURNAL OF GEOPHYSICAL RESEARCH, VOL. 113, E06S14, doi:10.1029/2007JE002995, 2008

Mineralogical composition of sands in Meridiani Planum determined from Mars Exploration Rover data and comparison to orbital measurements

A. D. Rogers[1,2] and O. Aharonson[1]

Received 22 August 2007; revised 16 January 2008; accepted 26 February 2008; published 6 May 2008.

[1] Constraints on the mineralogical composition of low-albedo, low-sulfur sands at Meridiani Planum are determined from Mars Exploration Rover (MER) Opportunity Miniature Thermal Emission Spectrometer (Mini-TES), Mössbauer, and Alpha Proton X–Ray Spectrometer measurements. Results of this work show that the sand is olivine basaltic in composition, with minor amounts of sulfate and a high-silica phase (glass or secondary amorphous silica). Measurements from all three instruments indicate that pyroxene is twice as abundant as olivine, and that the pyroxene composition is dominated by the low-calcium variety. The volume abundance of olivine is constrained to be 10–15%. Results from detailed analyses of MER data are used to ground truth the spectral emissivity and mineral abundances derived from orbit with Mars Global Surveyor TES data. TES-derived mineral abundances are within 5% of those derived from MER data, which is generally within the statistical errors associated with TES-derived phase abundances. The agreement lends support to global- and regional-scale variations in mineralogical composition determined from TES data in previous studies. An alternative method of least squares minimization is used for modeling the TES and Mini-TES data; the benefits of this method are demonstrated by comparison with conventional least squares techniques previously used by TES data users.

Citation: Rogers, A. D., and O. Aharonson (2008), Mineralogical composition of sands in Meridiani Planum determined from Mars Exploration Rover data and comparison to orbital measurements, *J. Geophys. Res.*, *113*, E06S14, doi:10.1029/2007JE002995.

1. Introduction

[2] Low-albedo regions of Mars are dominated by basaltic lithologies [e.g., *Soderblom*, 1992; *Mustard et al.*, 2005; *Christensen et al.*, 2000a; *Bandfield*, 2002; *Rogers and Christensen*, 2007]. One of these low-albedo regions, Meridiani Planum, has been investigated in detail by the Mars Exploration Rover (MER) Opportunity. The MER Athena science payload includes three spectrometers and a multispectral imager that provide complementary information about the composition of soils and rocks on the surface [*Squyres et al.*, 2003]. One of these instruments, the Miniature Thermal Emission Spectrometer (Mini-TES) [*Christensen et al.*, 2003] measures thermal infrared energy at a similar spectral sampling ($\sim$10 cm^{-1}) and range ($\sim$340–2000 cm^{-1}) to that of the Thermal Emission Spectrometer (TES, $\sim$10 cm^{-1} sampling and $\sim$200–1710 cm^{-1} range) [*Christensen et al.*, 2001] aboard the Mars Global Surveyor orbiting spacecraft. The similarity between the two instruments provides a unique opportunity for detailed surface-to-orbit comparisons.

[3] Mineralogical composition may be derived from thermal emission spectra [e.g., *Feely and Christensen*, 1999]; however, it is possible that nonunique solutions may arise. Mössbauer Spectrometer (MB) [*Klingelhöfer et al.*, 2003] data provide information on the distribution of iron in iron-bearing phases; however, this does not translate easily to mineral abundance because it is dependent on mineral compositions and the percentage of total iron. The Alpha Proton X–Ray Spectrometer (APXS) [*Rieder et al.*, 2003] provides elemental abundances; however, the partitioning of those elements into mineral phases is not known with certainty. Although each instrument has uncertainty associated with derived mineral abundance, they each may be used to constrain mineral abundance estimates from the other.

[4] The purpose of this study is threefold: first, to place narrow constraints on the volume abundance of plagioclase, pyroxene, olivine and other major phases present in basaltic sands at Meridiani Planum using combined information from the Mini-TES, APXS and MB instruments. Second, to compare the spectral emissivity and derived composition with that derived from TES data over Meridiani Planum. A similar study utilizing surface and orbital visible/near-infrared spectra from Pancam [*Bell et al.*, 2003] and Mars Express Observatoire pour la Mineralogie, l'Eau, les Glaces, et l'Activite (OMEGA) [*Bibring et al.*, 2005] was presented by *Arvidson et al.* [2006], and thus these

[1]Division of Geological and Planetary Sciences, California Institute of Technology, Pasadena, California, USA.
[2]Also at Department of Geosciences, State University of New York at Stony Brook, Stony Brook, New York, USA.

0148-0227/08/2007JE002995$09.00

Table 1. Mineral Abundance Estimates for Low-Albedo Surfaces in Meridiani Planum[a]

	Study								
	1 Orbit	2 Orbit	3[b] Orbit	4[c] Surface	5 Surface	6 Surface	7 Mini-TES	8 TES	9 TES Norm
Plagioclase	16	20	30	30	40	30	23 ± 4	18 ± 8	22 ± 10
Alkali Feldspar	12	5	–	–	–	–	4 ± 2	2 ± 2	2 ± 3
High-Ca Clinopyroxene	12	8	30	(20)	(35)	10	7 ± 4	4 ± 6	5 ± 7
Orthopyroxene	2	1	–	(20)	(35)	0	6 ± 3	4 ± 4	6 ± 5
Pigeonite	–	–	–	(20)	(35)	10	14 ± 4	12 ± 6	15 ± 7
Olivine	0	4	–	20	10	10	13 ± 2	7 ± 3	9 ± 4
Sulfate	12	5	–	0	[<5]	5	10 ± 0	8 ± 3	10 ± 4
Carbonate	6	–	–	–	–	5	2 ± 0	2 ± 1	2 ± 2
Opal and glasses	(8)	4	–	10	15	(20)	11 ± 6	8 ± 4	10 ± 5
Sheet-silicates	(8)	24	–	–	–	(20)	8 ± 2	10 ± 4	13 ± 6
Hematite	29	14	20	0	[<5]	–	0 ± 1	20 ± 2	0 ± 0
Other	0	15	15	15	–	10	2 ± 1	5 ± 8	6 ± 9

[a]Abundance in vol %. Parentheses/brackets indicate phases that were not distinguished in that particular study. For example, *Christensen et al.* [2004] (ref 4) reported 20% pyroxene, but did not distinguish pyroxene compositions. Dash means not reported. Study numbers: 1, *Bandfield* [2002]; 2, *Arvidson et al.* [2003]; 3, *Arvidson et al.* [2006]; 4, *Christensen et al.* [2004]; 5, *Yen et al.* [2005]; 6, *Glotch and Bandfield* [2006]; 7, this study, Mini-TES; 8, this study, TES; 9, this study, TES, normalized for hematite abundance (260–1301 cm^{-1} was range used).

[b]Grain size of phases: plagioclase = 100–200 μm, clinopyroxene = 20 μm, hematite = 200–400 μm, other (dust) = 10 μm.

[c]*Christensen et al.* [2004] assumed that all modeled sulfate (15%) and hematite (10%) were due to outcrop components mixed with sand. Their modal mineralogy was normalized for those phases and dust, and rounded to the nearest 5%.

data are not addressed here. Finally, the derived composition from this work is placed in global context by comparing the results to previous TES-derived abundance estimates for the major mineral groups in Meridiani and elsewhere [e.g., *Bandfield*, 2002; *Rogers and Christensen*, 2007]. Results from this study suggest that TES mineral determinations for this and other regions are likely accurate to within 5–10% in absolute abundance.

[5] Section 2 reviews previous estimates for the composition of sands in and around Meridiani Planum. Section 3 discusses the approach used to determine sand composition in this work, including an improved method of spectral deconvolution. Section 4 presents our results, and sections 5 and 6 conclude with a critical evaluation of the derived volume abundances of specific mineral groups (e.g., plagioclase, olivine, sulfates, pyroxene) and a discussion of the TES-derived mineral abundances of Meridiani Planum and other low-albedo regions.

2. Previous Estimates of Mineralogical Composition

2.1. Orbital Data Analyses

[6] From orbit, basaltic sands and hematite dominate the spectral signature measured by TES in Meridiani Planum [*Christensen et al.*, 2000a, 2001; *Glotch et al.*, 2004]. Pyroxene was identified as a mineralogic component of the Meridiani Planum surface layer in Phobos-II Imaging Spectrometer for Mars, Hubble Space Telescope and TES data [*Mustard et al.*, 1997; *Christensen et al.*, 2000a; *Murchie et al.*, 2000]. The presence of hydrated mineral(s) associated with the hematite deposit was suggested by *Baldridge and Calvin* [2004], based on analysis of Mariner 6 and 7 data; however, the level of hydration is weak compared to that associated with bright etched terrain units to the east of the hematite-rich plains [*Arvidson et al.*, 2005; *Gendrin et al.*, 2005; *Milliken et al.*, 2007; *Arvidson et al.*, 2006]. Spectral features due to hydrated minerals in the sulfate-rich outcrop analyzed by Opportunity are obscured in orbital observations of the hematite-rich unit due to partial cover from basaltic sands and hematite spherules [*Arvidson et al.*, 2006; *Milliken et al.*, 2007].

[7] Full modal mineralogical composition estimates for the surface of Meridiani Planum have been derived using TES [*Bandfield*, 2002; *Arvidson et al.*, 2003] and OMEGA data [*Arvidson et al.*, 2006]. Table 1 lists mineralogical compositions reported in those studies, for comparison. *Bandfield* [2002] derived global mineral distributions using TES data at a resolution of 1 pixel-per-degree (a pixel width of ~60 km at the equator). In that study, a few regions of mineralogical interest were discussed in detail, including Meridiani Planum. *Arvidson et al.* [2003] reported TES-derived composition for several geomorphic units in and around Meridiani Planum, including the hematite plains unit. Phase abundances derived in those two studies differ by up to 15%; however, each study extracted data from different regions within Meridiani Planum, therefore some of the differences could be due to surface variability. The discrepancies may also be attributed to differences between the spectral libraries used in each study. Finally, *Arvidson et al.* [2006] estimated mineral abundances of the Opportunity landing site from OMEGA spectra. Their stated detection limits for olivine and pyroxene abundances are < 5%, while limits for plagioclase, hematite and dust are ~10–20%. *Arvidson et al.* [2006] derive a composition that is dominated by subequal portions of plagioclase and clinopyroxene (diopside) at ~30% each, along with 20% hematite and 10% dust. They also note the absence of vibrational features between 1.0 and 2.5 μm associated with hydrated sulfates and phyllosilicates, indicating the lack of those particular phases on the surface. Finally, *Arvidson et al.* [2006] suggest that olivine could also be allowed as a viable phase. The preliminary work of *Wiseman* [2006] indicates that if olivine is present, its spectral features may be underrepresented in the OMEGA data due to increased backscattering of pyroxene crystals present on the plains [*Arvidson et al.*,

Table 2. Spectral Library[a]

Source	Phase Name
	Quartz Group
1	Quartz BUR-4120
	Alkali Feldspar Group
1	Microcline BUR-3460
	Plagioclase Group
1	Albite WAR-0235
1	Oligoclase BUR-060D
1	Andesine WAR-0024
1	Labradorite BUR-3080A
1	Bytownite WAR-1384
1	Anorthite BUR-340
	Orthopyroxene Group
1	Bronzite NMNH-93527
1	Enstatite HS-9.4B
1	Hypersthene NMNH-B18247
	Low-Ca Clinopyroxene Group
2	Average Lindsley pigeonite
	High-Ca Clinopyroxene Group
1	Diopside WAR-6474
1	Augite NMNH-9780
1	Augite NMHN-122302
1	Hedenbergite manganoan DSM-HED01
	Olivine Group
1	Forsterite BUR-3720A
1	Fayalite WAR-RGFAY01
3	KI 3362 Fo60[c]
3	KI 3115 Fo68[c]
3	KI 3373 Fo35[c]
3	KI 3008 Fo10[c]
	Phyllosilicates Group
1	Biotite BUR-840
1	Muscovite WAR-5474
1	Serpentine HS-8.4B
4	Illite Imt-1 < 0.2 μm (pellet)
1	Ca-montmorillonite solid STx-1
5	Saponite (Eb-1?) < 0.2 μm (pellet)
4	SWy-1 < 0.2 μm (pellet)
	Amorphous Silica Group
6	K-rich glass
6	SiO_2 glass
7	Opal-A (01–011)
8	Al-opal
	Amphibole Group
1	Magnesiohastingsite HS-115.4B
1	Magnesiohornblende WAR-0354
	Oxide Group
9	Average Meridiani and Aram hematite (TT derived)[b]
9	Magnetite MTS4[b]
	Sulfate Group
1	Anhydrite ML-S9[b]
1	Gypsum ML-S6[b]
10	Natrojarosite LNVJAR1-R1
10	Kieserite KIEDE1[b]
	Carbonate Group
1	Calcite C40
1	Dolomite C20
	Shocked Plagioclase Group
11	Shocked An 22.6 GPa[d]
11	Shocked An 56.3 GPa[d]

2006]. The addition of dust to the mixture could also serve to increase the olivine obscuration [*Arvidson et al.*, 2006].

2.2. MER Data Analyses

[8] Measurements of undisturbed, hematite-poor soil targets in Eagle Crater were used for initial analyses of Meridiani sand composition. These analyses suggested an olivine basaltic composition [*Bell et al.*, 2004; *Christensen et al.*, 2004; *Klingelhöfer et al.*, 2004; *Rieder et al.*, 2004], with varying amounts of fine-grained dust and possibly additional glass and oxide components [*Christensen et al.*, 2004]. Inside Endurance Crater, the Opportunity payload was used to investigate the target dubbed "Auk" [*Yen et al.*, 2005], which is a relatively dust-free patch of sand. Measurements of Auk are also consistent with an olivine basaltic composition. Finally, *Glotch and Bandfield* [2006] derived a basaltic sand end-member from the Opportunity Mini-TES data set using factor analysis and target transformation techniques [*Malinowski*, 1991; *Bandfield et al.*, 2000a], and presented a preliminary mineralogical composition derived from that end-member that also is consistent with olivine basalt.

3. Methods

3.1. Overview

[9] Although several previous studies have addressed the composition of the ubiquitous sand component at Meridiani (section 2), the approach used in this work is distinguished from those studies by three aspects: (1) an isolated basaltic end-member [*Glotch and Bandfield*, 2006] is used for derivation of composition, (2) an alternative method of least squares fitting is used to achieve improved fits to the Mini-TES spectra, and (3) phases are alternately included and excluded from the spectral library used by the model, and each mineralogical result is converted to chemical composition and iron distribution for comparison with APXS and MB measurements of low-dust basaltic sands. The use of multiple data sets is a significant improvement in that the complementary information may be used to converge on a robust answer and also to eliminate solutions that do not satisfy all of the constraints.

[10] Our general procedure for deriving the best constrained composition from the Mini-TES basalt end-member is as follows. A standard spectral library consisting of minerals, mineraloids, and glasses is constructed (Table 2). The library is used to find the least squares fit to the Mini-TES spectrum and derive a mineralogical composition (section 3.2). In order to assess the relative importance of each mineral group (e.g., plagioclase, orthopyroxene, oliv-

Notes to Table 2:

[a]Mineral spectra are from (1) the ASU spectral library available online at http://tes.asu.edu [*Christensen et al.*, 2000]; (2) *Wyatt et al.* [2001]; (3) provided by V. E. Hamilton; (4) *Michalski et al.* [2006]; (5) *Michalski et al.* [2005]; (6) *Wyatt et al.* [2001]; (7) *Michalski et al.* [2003]; (8) provided by M. D. Kraft; (9) *Glotch et al.* [2004]; (10) provided by R. V. Morris; (11) spectra described by *Johnson et al.* [2002]. Chemical abundances associated with each spectrum are from the ASU library or the above references, except where indicated by a footnote.

[b]Chemical abundances calculated from pure structural formula.

[c]Described by *Morse* [1996].

[d]See text for source of chemical information.

ine) to the overall spectral fit and derived chemistry, groups are then alternately excluded from the standard library and the Mini-TES spectrum is remodeled. For each model result, the corresponding mineralogical composition is converted to chemical composition and iron distribution to facilitate direct comparison with APXS and MB measurements of undisturbed soils (section 3.4).

3.2. Linear Least Squares Analysis

3.2.1. Overview

[11] *Glotch and Bandfield* [2006] applied factor analysis and target transformation techniques [*Malinowski*, 1991; *Bandfield et al.*, 2000a] to Mini-TES spectra from the first 350 sols of the Opportunity mission in an effort to determine the number of independently varying components within that data set and their corresponding spectral shapes. They identified six components: hematite, basaltic sand, dust, outcrop, and two atmospheric dust opacity shapes. This work presents a detailed analysis of the basaltic sand end-member derived by *Glotch and Bandfield* [2006]. The Mini-TES end-member is used for modeling because (1) it is most representative of the average basaltic sand observed by Opportunity, and presumably, of Meridiani Planum sands observed from orbit, and (2) the basalt shape is free of influence from dust, outcrop, hematite, and atmospheric components.

[12] The sand end-member derived by *Glotch and Bandfield* [2006] has an emissivity "peak" at 8 μm, where emissivity values rise above 1.0. At wavelengths <8 μm, the emissivity continuum abruptly flattens out and does not decrease by more than 0.01 emissivity. This spectral behavior is not observed in laboratory spectra of either coarse particulate (here, meaning >63 μm) or fine-particulate basalt. Though fine-particulate silicates do exhibit a gradual decrease in emissivity from the Christiansen frequency toward shorter wavelengths [e.g., *Lyon*, 1965; *Conel*, 1969], abrupt stair-step decreases in emissivity are not observed. Thus we conclude that the emissivity feature at 8 μm is not a high peak relative to a short-wavelength "rolloff" (which would imply dust contamination), but rather is an artifact of the target transformation process. Emissivity near 8 μm is likely exaggerated to slightly higher values relative to the rest of the spectrum. Further support for the suggestion that the $\sim$8 μm peak is exaggerated comes from an assessment of the materials from which the basaltic shape was derived. The presence of residual dust in the basaltic shape derived from factor analysis and target transformation would require that the dust be present at constant abundance within the sand. This is unlikely, given the wide variety of surfaces (dunes, sand patches, and plains) over which the basaltic sand occurs and from which Mini-TES spectra were acquired. Pancam albedo values from Endurance crater bed forms and from plains bed forms encountered between Eagle and Endurance craters range between 0.11 and 0.17 [*Bell et al.*, 2008], indicating that dust and sand proportions are not constant.

[13] To estimate the mineralogical composition from TES spectra, and from the Mini-TES basaltic end-member derived by *Glotch and Bandfield* [2006], we employ linear least squares fitting techniques similar to that of *Ramsey and Christensen* [1998] with a spectral library composed of common igneous and secondary minerals. Atmospheric end-members derived by *Bandfield et al.* [2000a] and *Bandfield* [2002] are also used in the TES data analysis. In the least squares fitting technique of *Ramsey and Christensen* [1998], spectra with negative percentages are iteratively removed from the library until only those with positive percentages remain in the solution. With this procedure, it is possible (1) that only a local minimum error solution may be found and (2) that a correct end-member could be prematurely discarded in the iterative process [e.g., *Bandfield et al.*, 2000b; *Seelos and Arvidson*, 2003; *Rogers and Christensen*, 2007]. The nonnegative least squares method we employ in this work [*Lawson and Hanson*, 1974, p. 61; *Seelos and Arvidson*, 2003] differs in that all spectra remain in the design matrix and are available to the solution until the final, nonnegative solution is reached. Two sets of spectral coefficients, which may be positive or zero, are maintained as the algorithm converges toward the best fit solution. The coefficients are each tested for nonnegativity and included into these sets, finding the best fit least squares solution at each step. If any newly added end-member causes the set of previously indexed positive coefficients to become negative, then the coefficients are incrementally adjusted until all coefficients in the positive set become nonnegative again. Using the new set of end-members, the best fit solution vector is again found. Iterations continue in this fashion until all coefficients are zero or positive, and no additional coefficients can be introduced with positive values. Refer to *Lawson and Hanson* [1974] for details. Our implementation of the algorithm does allow atmospheric and blackbody end-member coefficients to be negative, as does the method of *Ramsey and Christensen* [1998], following *Bandfield et al.* [2000b].

[14] The two least squares algorithms are hereafter referred to as the iterative library reduction (ILR) and modified nonnegative (MNN) methods. Results from TES spectral models are presented using both methods. Because in our approach the Mini-TES spectral analysis involves alternately excluding mineral phases from each model run, only results using the MNN algorithm are reported.

3.2.2. Least Squares Algorithm Comparison

[15] Methods similar to MNN least squares have been relatively underutilized in modeling TES and Mini-TES spectra [*Seelos and Arvidson*, 2003]. Thus, before applying the MNN fitting technique to spectra from Mars, we first tested the accuracy of the technique on laboratory spectra of a suite of 96 rocks whose modes were previously estimated from traditional petrographic methods [*Feely and Christensen*, 1999]. For comparison, we also modeled the laboratory spectra using the ILR technique. Errors on the petrographically determined modes were estimated to be $\pm$5–15% [*Feely and Christensen*, 1999]. The spectral library utilized by *Feely and Christensen* [1999] is used for the model comparison; ten additional spectra of phases potentially present in the suite of rocks (antigorite, bytownite, Ca-montmorillonite, illite, crystalline heulandite, pigeonite, three olivine solid solution compositions, and K-rich silica glass) were also included in the library. Model fits were limited to the 400–1600 cm^{-1} spectral range to be consistent with the work of *Feely and Christensen* [1999]. Finally, the models are compared using

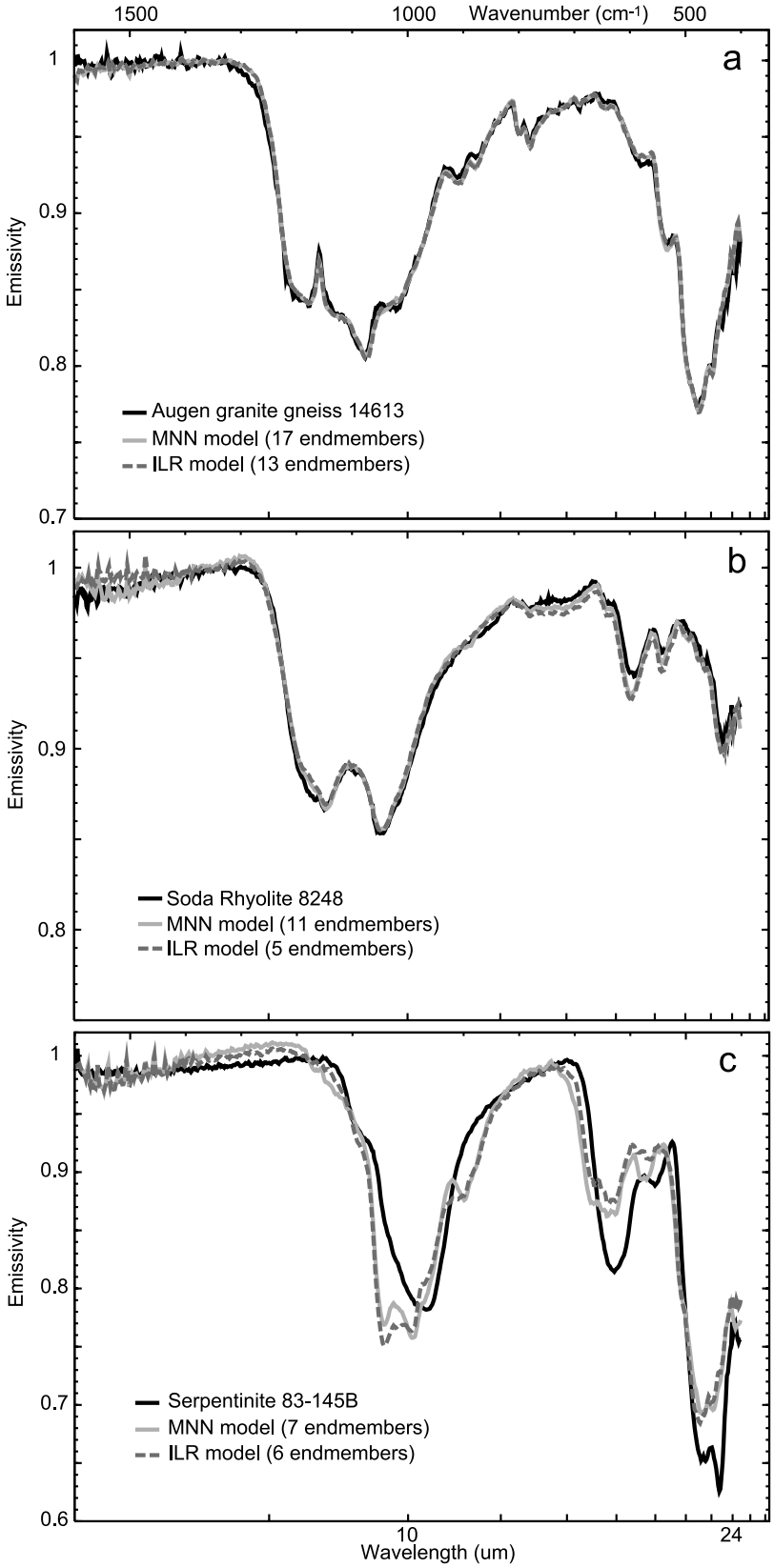
1500
1000
Wavenumber (cm-1)
500
a
Emissivity
Augen granite gneiss 14613
MNN model (17 endmembers)
ILR model (13 endmembers)
b
Soda Rhyolite 8248
MNN model (11 endmembers)
ILR model (5 endmembers)
c
Serpentinite 83-145B
MNN model (7 endmembers)
ILR model (6 endmembers)
Wavelength (um)
10
24

Figure 1

spectral samplings of both 2 cm^{-1} and 10 cm^{-1} (laboratory sampling and TES/Mini-TES sampling, respectively).

[16] As discussed above, all library spectra are available to the solution during the MNN optimization process. This ensures that a global minimum error solution is always found. Indeed, the MNN method produced identical or lower RMS values than the ILR method for every rock spectrum. For the 2 cm^{-1} data, the MNN least squares usually produces negligible RMS improvements over ILR. Typically these improvements are achieved through the use of one to five additional library spectra at insignificant fractions (<1%). Figure 1a shows typical model fits for MNN and ILR at 2 cm^{-1} sampling, where the two methods provide nearly identical fits for 95% of the spectra, based on visual inspection. For ~5% of the spectra tested, the MNN model provides modest improvement in the fit to the spectrum (Figure 1b). The models yield modal abundances within 5% of each other for 75% of the cases, and diverged by more than 15% for one spectrum. However, in that example, neither model produced a satisfactory fit to the mixed spectrum (Figure 1c). This can be attributed to one or more missing end-members from the spectral library.

[17] In contrast to the 2 cm^{-1} data, model results diverge more commonly for mixed spectra and library spectra that are degraded to 10 cm^{-1} sampling. For approximately 80% of the spectra, the two models produced nearly identical fits (Figure 2a). A few (~5%) of the overall model fits from MNN least squares were slightly improved over the ILR model, based on lower RMS errors and visual inspection of the fits (Figure 2b); phase abundances for those cases differ by < 10% between models. In three examples, it is apparent that a correct end-member was prematurely discarded by the ILR method, based on the difference in fit between the ILR and MNN methods (Figure 2c). However, for approximately 5% of the spectra, the MNN method used an obviously incorrect end-member (in these cases, calcite) at low abundance to reduce the overall RMS error (Figure 2d). These abundances are always well below the detection limit, however, and therefore may be safely disregarded. In addition, it is important to note that the ILR model is also subject to the use of incorrect end-members at low abundance [e.g., *Feely and Christensen*, 1999]. Finally, the remaining spectra (~5%) were not fit well by either model.

[18] With the exception of those spectra that are not fit well by either model (likely due to one or more missing end-members from the spectral library), only six spectra showed more than 10% difference in one or more phase abundances between the two models. For those six, the MNN least squares modeled abundances are not further from the known (petrographic) values than the ILR, within the stated petrographic errors of ~5–15%. In two cases, the MNN-derived phase abundances are closer to the known values by 15% or more. We note that although model fits were nearly identical for > 80% of the cases, derived phase abundances differ by more than 5% between models for ~45% of the cases. Phase abundances differ by more than 10% for ~20% of the cases. This suggests that each model commonly used a slightly different combination of spectra at the ~5–10% level to achieve a similar modeled spectrum and fit, and illustrates the potential for nonunique solutions with either of these methods.

3.2.3. Summary

[19] The analysis above indicates that the MNN least squares method is generally more reliable than the ILR method. Where the number of spectral channels is large relative to the number of library spectra, as was the case with the 2 cm^{-1} sampled data, the models are nearly identical. However, as the number of library spectra approaches the number of channels (e.g., 10 cm^{-1} sampled data), the models more commonly diverge. Because the MNN technique is mathematically more robust, and finds a global minimum, the RMS error value is always equal to or less than that of the ILR method. With both techniques, there is potential for an incorrect end-member to be introduced at low abundance (Figure 2d); however, these abundances are usually below the estimated detection limit and thus are disregarded. For the 10 cm^{-1} data, there are three examples (out of 96 spectra) where it is apparent that a correct end-member was prematurely discarded by the ILR method (Figure 2c). This confirms that where there is a large number of library spectra relative to the number of channels, premature exclusion of a correct end-member using the ILR method is more likely to occur. Conversely, an increase in library size should not result in correct end-member exclusion using the MNN technique. Similarly, in modeling TES spectra with the ILR method, *Rogers and Christensen* [2007] discussed rare cases where increasing the size of the library by one or more spectra would cause an increase in RMS error. An additional advantage of using the MNN least squares model is that the number of library spectra does not adversely affect the ability to find the minimum error solution. These examples demonstrate the value of using library-preserving optimization techniques to derive mineralogical composition and verify results [e.g., *Seelos and Arvidson*, 2003; *Staid et al.*, 2004; *Johnson et al.*, 2006; *Noe Dobrea et al.*, 2006].

3.3. Statistical Errors on Derived Mineral Abundance

3.3.1. Calculating Statistical Errors

[20] Using the MNN and ILR least squares algorithms (section 3.2), we solve for the vector (hereafter, ''library spectra'') coefficients that minimize the difference between the measured and reconstructed spectrum. The coefficients are allowed to be positive or zero; for atmospheric or

Figure 1. Comparison of model fits to spectra acquired at 2 cm^{-1} sampling using MNN and ILR least squares. (a) Example of typical case (95% of the spectra), where the two models produce nearly identical model fits and derived composition. (b) Example of the rare case where the MNN model provides modest improvement in the fit to the spectrum (e.g., between ~500–800 cm^{-1} and ~1150–1200 cm^{-1}). The difference in derived composition is 4% feldspar. (c) The only case where the two models diverged by >15% in derived composition for one or more phases. Neither model provides a satisfactory fit to the serpentinite spectrum, however, suggesting that a correct end-member is missing from the input library (Table 3).

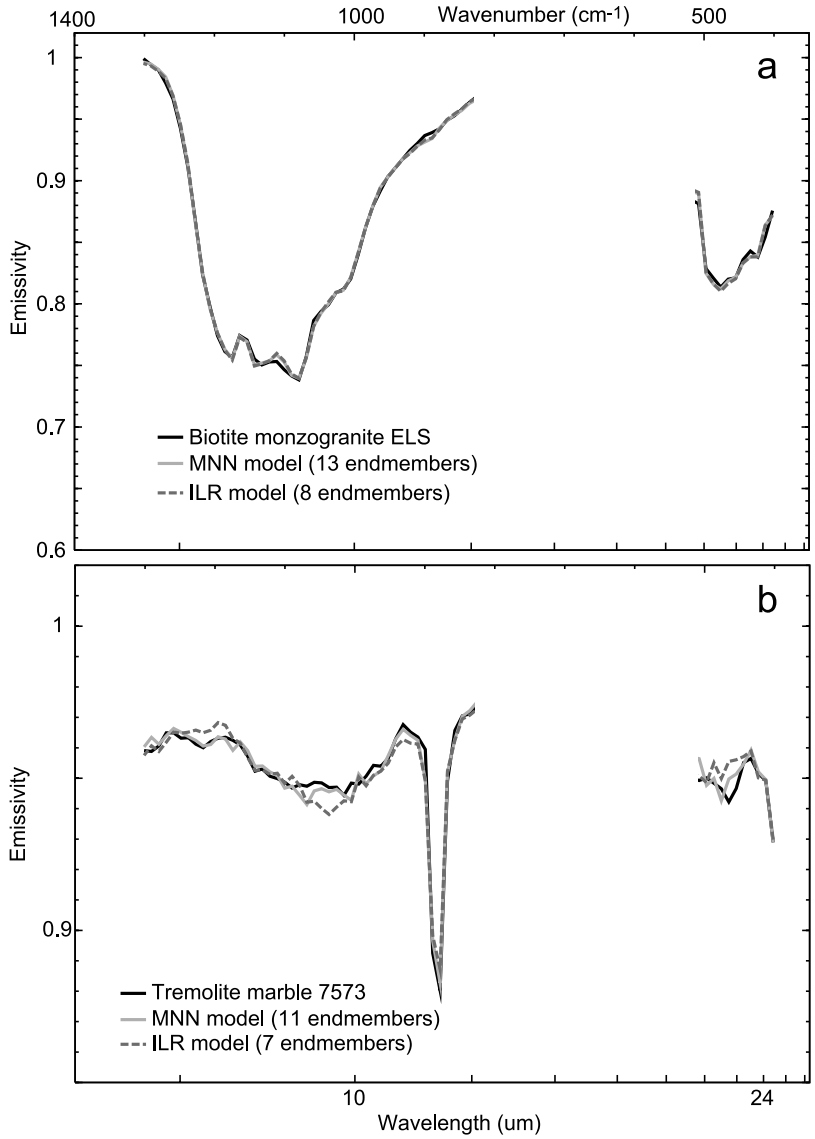

Figure 2. Comparison of model fits to spectra acquired at 10 cm^{-1} sampling using MNN and ILR least squares. Within the stated petrographic errors of ~10–15%, the MNN least squares model is never further from the known values than the ILR. In a few instances, the MNN is closer to the known values by 20% or more. (a) Example of typical case (~80% of the spectra), where the two models produce nearly identical model fits. The derived phase abundances for ~65% of these cases match to within 5%. Phase abundances for three of the examples differ by more than 10%. For two of these three cases, the MNN least squares model produced phase abundance values at least 10% closer to the known values than the ILR least squares. (b) Example of instances (~5% of the spectra) where the MNN model provides modest improvement in the fit to the spectrum. Phase abundances for these cases differ by less than 10% between the two models. (c) Example of instances (~5% of the spectra) where the MNN model provides a better fit than the ILR model, across the entire spectral range. The relatively poor fit from the ILR model suggests that a correct end-member (in this example, sanidine SALS-1s) was ejected during the iterative process. (d) Example of instances (~5% of the spectra) where the MNN model used an incorrect end-member at low abundance to achieve the lowest possible RMS error. In this case, 9% calcite was used to achieve a better fit between 1050 and 1150 cm^{-1} and 450–500 cm^{-1}; however, the prominent mismatch at ~890 cm^{-1} (arrow) indicates that calcite is not actually present.

blackbody spectra, coefficients may also be negative. Library spectra with nonzero coefficients are the final "end-members" of the solution. We calculate an estimated $m \times m$ coefficient covariance matrix V where m is the number of end-members. If X is the set of final end-member spectra, and Y is the mixed spectrum, then

$$V = \left(\frac{Y^T Y - b^T X^T Y}{f}\right)\left(X^T X\right)^{-1} \quad (1)$$

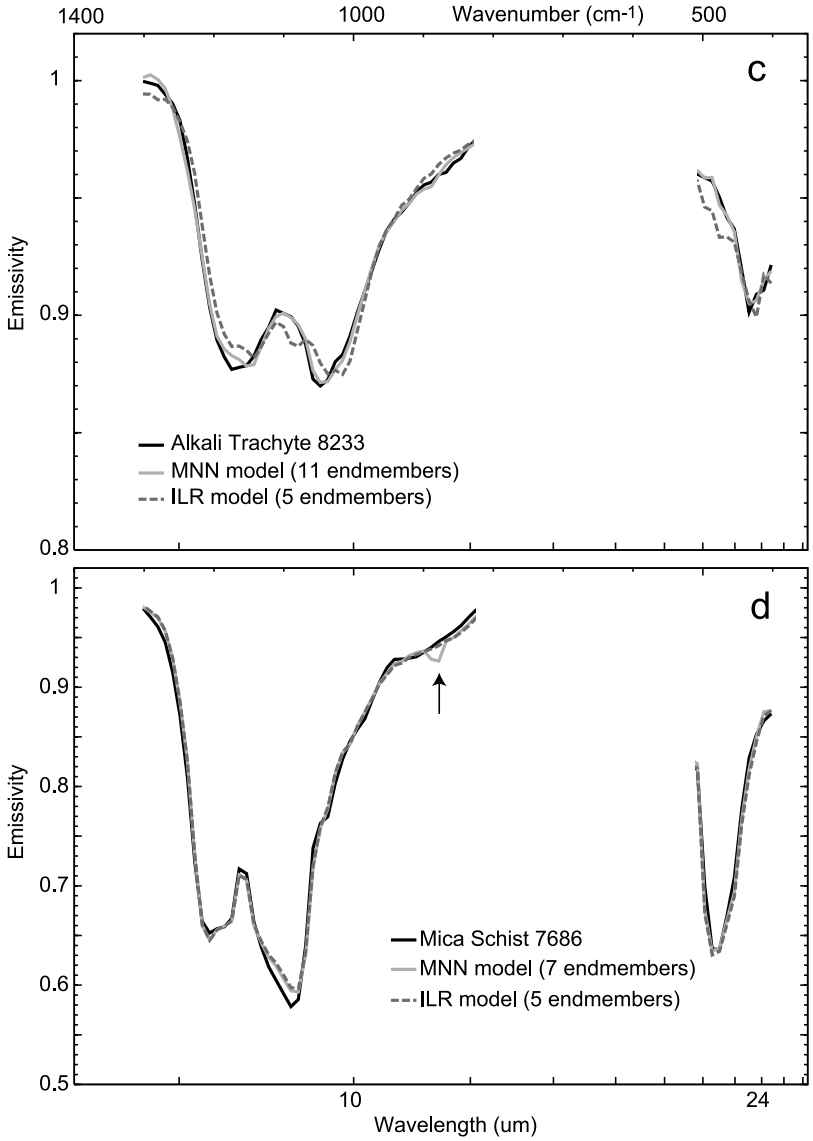

Figure 2. (continued)

where f equals the number of channels minus the number of end-members m and b is the column of nonzero coefficients, which has length m. The T denotes matrix transpose. Statistical errors (σ) associated with each coefficient in b are taken from the square root of the diagonal of the covariance matrix V.

3.3.2. Interpreting Statistical Errors

[21] The statistical errors for each end-member will vary depending on the other end-members in the solution. Errors are highest for end-members that are similar in spectral shape to other end-members present in the solution. For example, if two labradorite end-members are found in the final solution, the uncertainties associated with each of the labradorite coefficients will be high relative to the case where only one labradorite end-member is found. This is due to the redundancy of the two labradorites; the high error associated with each indicates that these end-members may be used interchangeably. Correspondingly, the covariance value between these end-members will be strongly negative. However, the error associated with the total abundance of labradorite is much lower (the amount of error reduction depends on the covariance value) than that associated with the individual labradorite end-members. In other words, the total abundance of labradorite is better constrained than the individual labradorite end-member abundances. Taking this a step further, the total abundance of plagioclase, or other phases that are spectrally similar to labradorite, is better constrained than the total abundance of labradorite.

[22] In this work, end-members with positive coefficients are grouped by mineral class and spectral similarity, and the total error is reported for each group using the standard error propagation equation [e.g., *Meyer*, 1997; *Bevington and*

Table 3. Composition of Low-Sulfur, Low-Albedo Soil Targets[a]

Target Name	Na_2O	Na_2O AA	MgO	MgO AA	Al_2O_3	Al_2O_3 AA	SiO_2	SiO_2 AA	SO_3	SO_3 AA	Cl	Cl AA	K_2O	K_2O AA	CaO	CaO AA	TiO_2	TiO_2 AA	FeO	FeO AA	Ol, %	Ol AA	Px, %	Px AA	Mt, %	Mt AA	npOx, %	npOx AA	Hm, %	Hm AA
Tarmac	1.8	*0.2*	7.6	*1.3*	9.3	*0.7*	46.3	*1.6*	5.0	*0.7*	0.6	*0.1*	0.5	*0.1*	7.3	*0.6*	1.0	*0.2*	18.8	*1.1*	39	*2*	37	*2*	6	*3*	14	*2*	4	*3*
Soil_Millstone_Dahlia	2.4	*0.2*	7.1	*1.2*	10.0	*0.7*	47.7	*1.7*	5.2	*0.7*	0.6	*0.1*	0.5	*0.1*	7.3	*0.6*	0.8	*0.2*	16.6	*1.0*	38	*2*	40	*2*	5	*3*	14	*2*	3	*3*
Auk_RAT	2.4	*0.2*	6.9	*1.2*	10.4	*0.7*	48.8	*1.7*	4.6	*0.6*	0.6	*0.1*	0.6	*0.1*	7.4	*0.6*	0.8	*0.2*	15.9	*0.9*	38	*2*	40	*2*	6	*3*	14	*2*	1	*3*
Rocknest_void_soil	2.4	*0.2*	7.7	*1.3*	9.6	*0.7*	46.7	*1.6*	4.6	*0.7*	0.6	*0.1*	0.5	*0.1*	7.3	*0.6*	0.9	*0.2*	18.0	*1.0*	40	*2*	47	*2*	7	*3*	13	*2*	3	*3*
Fala	2.2	*0.2*	7.5	*1.3*	8.9	*0.6*	45.6	*1.6*	4.9	*0.7*	0.6	*0.1*	0.5	*0.1*	7.5	*0.6*	0.9	*0.2*	19.6	*1.1*	-	-	-	-	-	-	-	-	-	-
Average	2.2	*0.2*	7.3	*1.3*	9.6	*0.7*	47.0	*1.6*	4.9	*0.7*	0.6	*0.1*	0.5	*0.1*	7.4	*0.6*	0.9	*0.2*	17.8	*1.0*	39	*2*	41	*2*	6	*3*	14	*2*	3	*3*

[a]Chemical abundances (wt %) are from R. Gellert et al. (Chemistry along the traverse of Opportunity at Meridiani Planum: Salty outcrops, spherules, soils, and more, manuscript in preparation, 2008). Iron-bearing phase assignments are from Table 3 of *Morris et al.* [2006]. Numbers in italics are the absolute accuracy associated with each measurement. Chemical abundances do not add to 100 because P_2O_5, Cr_2O_3, and MnO are not shown. AA, absolute accuracies.

Robinson, 2003, p. 41]. For example, to calculate the total error (σ_T) associated with the summed coefficients of three end-members (e_1, e_2, e_3), the equation is given by

$$\sigma_T^2 = \sigma_{e1}^2 + \sigma_{e2}^2 + \sigma_{e3}^2 + 2\sigma_{e1,e2} + 2\sigma_{e2,e3} + 2\sigma_{e1,e3}, \quad (2)$$

where $\sigma_{e1,e2}$ is the covariance of the first two end-members being grouped, $\sigma_{e2,e3}$ is the covariance of the second and third end-members being grouped, and so on. If four end-members were being grouped, then an additional four terms would be added to the right side of (2): σ_{e4}^2, $2\sigma_{e1,e4}$, $2\sigma_{e2,e4}$, and $2\sigma_{e3,e4}$. For this work, the spectral groups are user-defined based on a priori knowledge of mineral classes and spectral similarity. In theory, the covariance values could be used to define spectral groups; however, the grouping would depend on the mixed spectrum and the input library. Thus if covariance values are used to define groups, the group definitions could change with each new mixed spectrum or spectral library. Interpreting results from observations with continually shifting group definitions would not be a straightforward process.

[23] Statistical errors are not direct indicators of the quality of spectral fit. For example, if a library of two spectra are used to model a mixed spectrum, and those two spectra are not true end-members, the model fit will be poor. However, the statistical error on the derived abundance of those spectra will be low. Thus the statistical error for modeled phase abundances cannot be used instead of RMS error or visual inspection to evaluate the quality of the model fit. Likewise, the statistical errors cannot be used alone to evaluate the likely presence of a particular end-member; the quality of the model fit must also be evaluated.

[24] Several factors contribute to the errors associated with derived phase abundances, phase detectability, and to the quality of spectral fits. These include the number of channels used for modeling, the number of library spectra input to the model, the number of correct end-members present in the input library, the natural spectral contrast of the mineral, the other minerals that are present with the mineral of interest, and the signal-to-noise ratio of the mixed spectrum and library. A detailed treatment of phase abundance errors as well as empirically determined, generalized detection limits for thermal emission spectroscopy are also given by *Ramsey and Christensen* [1998], *Feely and Christensen* [1999], *Christensen et al.* [2000b], *Wyatt et al.* [2001], *Hamilton et al.* [2001], and *Noe Dobrea et al.* [2006].

3.4. Chemical Composition and Iron Distribution From Mini-TES

[25] For each mineralogical composition that is output from the model, the associated chemical composition is calculated using the method employed by *Hamilton and Christensen* [2000], *Wyatt et al.* [2001], *Hamilton et al.* [2001], and *McSween et al.* [2003]. First, the concentration of each end-member is normalized for blackbody contribution to produce abundance values. The abundance is assumed to be volume percentage [*Feely and Christensen*, 1999; *Bandfield et al.*, 2000b; *Hamilton and Christensen*, 2000]. The volume percent of each end-member is converted to weight percent (wt %) by dividing by the density associated with that mineral/phase and renormalizing to 100%. Next, the known wt % oxides for each end-member

Table 4. Mini-TES-Derived Mineralogical Composition, Chemical Composition, and Iron Distribution

	Full	No Alk Feld	No Amphibole	No Carbonate	No Hi-Ca pyx
Derived abundances, vol %					
Quartz	0 ± 0	0 ± 0	0 ± 0	0 ± 0	0 ± 0
Alkali Feldspar	5 ± 2	0 ± 0	5 ± 2	3 ± 2	3 ± 2
Plagioclase	20 ± 6	26 ± 8	23 ± 5	14 ± 9	15 ± 4
Orthopyroxene	7 ± 3	7 ± 4	8 ± 2	2 ± 2	9 ± 3
Pigeonite	12 ± 5	12 ± 5	9 ± 4	18 ± 4	15 ± 5
High-Ca clinopyroxene	8 ± 3	5 ± 4	9 ± 3	4 ± 3	0 ± 0
Olivine	14 ± 2	13 ± 3	14 ± 3	15 ± 2	17 ± 2
Sheet-silicates	6 ± 3	8 ± 3	7 ± 3	2 ± 3	8 ± 3
Opal and glasses	12 ± 6	15 ± 7	12 ± 2	22 ± 6	16 ± 7
Amphibole	3 ± 2	1 ± 1	0 ± 0	3 ± 2	2 ± 1
Oxides	0 ± 0	0 ± 2	0 ± 0	5 ± 2	2 ± 2
Sulfate	10 ± 1	10 ± 2	10 ± 1	10 ± 1	11 ± 1
Carbonate	2 ± 1	2 ± 1	2 ± 1	0 ± 0	2 ± 1
Shocked feldspar	0 ± 0	2 ± 5	0 ± 5	2 ± 10	2 ± 6
Derived abundances, wt %					
Quartz	0 −0/+0	0 −0/+0	0 −0/+0	0 −0/+0	0 −0/+0
Alkali Feldspar	4 −1/+2	0 −0/+0	4 −1/+1	3 −0/+0	2 −1/+0
Plagioclase	18 −12/+6	24 −24/+1	20 −4/+3	12 −12/+5	13 −1/+3
Orthopyroxene	8 −2/+2	8 −8/+5	10 −3/+4	3 −2/+0	10 −4/+7
Pigeonite	14 −3/+3	14 −5/+14	10 −2/+0	20 −7/+12	16 −5/+9
High-Ca clinopyroxene	9 −2/+3	5 −2/+0	10 −4/+1	4 −4/+2	0 −0/+0
Olivine	18 −0/+1	17 −0/+7	18 −2/+3	19 −6/+9	21 −12/+5
Sheet-silicates	5 −3/+1	7 −1/+7	6 −5/+1	1 −1/+2	7 −5/+3
Opal and glasses	10 −0/+2	11 −5/+0	10 −4/+6	16 −3/+0	12 −4/+0
Amphibole	3 −3/+2	1 −1/+0	0 −0/+0	3 −1/+0	2 −0/+0
Oxides	0 −0/+0	0 −0/+1	0 −0/+0	9 −2/+2	3 −3/+3
Sulfate	8 −3/+6	8 −3/+13	8 −3/+5	8 −3/+5	8 −3/+7
Carbonate	2 −0/+1	2 −0/+2	2 −0/+1	0 −0/+0	2 −1/+1
Shocked feldspar	0 −0/+0	4 −4/+2	0 −0/+4	3 −3/+11	3 −3/+3
Modeled Iron distribution, % Fe in					
Olivine	54 −8/+10	51 −7/+2	57 −8/+10	31 −3/+3	49 −16/+0
Pyroxene	43 −11/+11	45 −11/+8	40 −10/+10	31 −0/+2	36 −14/+29
Magnetite	0 −0/+0	0 −0/+0	0 −0/+0	36 −4/+0	8 −8/+9
Hematite	0 −0/+0	1 −1/+8	0 −0/+0	0 −0/+0	5 −5/+4
Phyllosilicate	2 −1/+1	2 −0/+1	3 −2/+0	0 −0/+1	1 −1/+1
Amphibole	1 −1/+1	0 −0/+0	0 −0/+0	1 −1/+0	1 −0/+0
Carbonate	0 −0/+0	0 −0/+0	0 −0/+0	0 −0/+0	0 −0/+0
Plagioclase	0 −0/+0	1 −1/+0	0 −0/+1	0 −0/+2	1 −0/+0
olv/pyx	1 −0/+1	1 −0/+0	1 −0/+1	1 −0/+0	1−1/+1
Chemistry (H_2O- and CO_2-free), wt %					
SiO_2	48 −3/+2	50 −9/+1	48 −1/+0	47 −6/+3	48 −3/+0
Al_20_3	10 −4/+2	12 −8/+1	11 −1/+2	8 −6/+5	9 −1/+1
FeO	15 −0/+0	14 −0/+5	15 −3/+2	24 −6/+9	20 −2/+2
MgO	10 −2/+3	10 −1/+4	10 −2/+2	9 −2/+2	11 −1/+0
CaO	9 −1/+1	8 −1/+3	9 −0/+1	7 −0/+1	7 −1/+3
Na_2O	1 −0/+0	2 −1/+0	1 −0/+0	1 −1/+1	1 −0/+0
MnO	0 −0/+0	0 −0/+0	0 −0/+0	0 −0/+0	0 −0/+0
K_2O	1 −0/+0	1 −0/+0	1 −0/+0	1 −0/+0	1 −0/+0
TiO_2	0 −0/+0	0 −0/+0	0 −0/+0	0 −0/+0	0 −0/+0
SO_3	4 −1/+3	4 −2/+7	4 −1/+2	4 −1/+3	4 −2/+3
H_2O (unnormalized)	2 −1/+0	2−1/+0	2 −1/+0	2−2/+0	2 −2/+0
CO_2 (unnormalized)	1 −0/+2	1−0/+4	1 −0/+2	0 −0/+3	1 −0/+2

	No High-Si	No Lo-Ca Pyx	No Opx	No Opal/Glass	No Pigeonite
Derived abundances, vol %					
Quartz	1 ± 0	1 ± 1	0 ± 0	1 ± 1	0 ± 1
Alkali Feldspar	9 ± 2	7 ± 2	5 ± 2	6 ± 2	5 ± 2
Plagioclase	13 ± 4	26 ± 4	20 ± 7	14 ± 4	25 ± 4
Orthopyroxene	0 ± 0	0 ± 0	0 ± 0	3 ± 3	11 ± 2
Pigeonite	22 ± 3	0 ± 0	17 ± 4	19 ± 4	0 ± 0
High-Ca clinopyroxene	16 ± 2	18 ± 3	11 ± 4	8 ± 5	10 ± 4
Olivine	10 ± 2	10 ± 2	12 ± 4	11 ± 2	13 ± 2
Sheet-silicates	0 ± 0	8 ± 4	5 ± 4	12 ± 3	8 ± 3
Opal and glasses	0 ± 0	17 ± 6	13 ± 8	0 ± 0	14 ± 2
Amphibole	2 ± 1	1 ± 1	4 ± 2	1 ± 1	0 ± 1
Oxides	0 ± 0	0 ± 0	0 ± 3	0 ± 0	0 ± 0
Sulfate	8 ± 1	9 ± 1	10 ± 1	10 ± 2	10 ± 1
Carbonate	2 ± 1	3 ± 1	1 ± 1	2 ± 1	3 ± 1
Shocked feldspar	18 ± 4	0 ± 0	3 ± 6	13 ± 4	0 ± 0
Derived abundances, wt %					
Quartz	1 −0/+0	1 −1/+0	0 −0/+0	1 −0/+0	0 −0/+0
Alkali Feldspar	7 −1/+2	6 −1/+1	4 −1/+2	5 −1/+2	5 −1/+0

Table 4. (continued)

	No High-Si	No Lo-Ca Pyx	No Opx	No Opal/Glass	No Pigeonite
Plagioclase	10 −6/+6	24 −4/+7	18 −13/+1	12 −0/+1	22 −1/+3
Orthopyroxene	0 −0/+0	0 −0/+0	0 −0/+0	3 −3/+3	13 −3/+3
Pigeonite	22 −5/+8	0 −0/+0	19 −7/+14	20 −6/+13	0 −0/+0
High-Ca Clinopyroxene	16 −12/+5	22 −4/+6	12 −4/+5	8 −8/+4	12 −1/+0
Olivine	11 −1/+2	14 −1/+0	15 −0/+9	13 −11/+5	18 −5/+3
Sheet-silicates	0 −0/+0	8 −4/+3	4 −2/+0	9 −7/+1	7 −4/+3
Opal and glasses	0 −0/+0	13 −11/+7	10 −10/+2	0 −0/+0	12 −3/+5
Amphibole	1 −1/+1	1 −1/+1	4 −1/+1	1 −1/+0	0 −0/+1
Oxides	0 −0/+0	0 −0/+0	0 −0/+3	0 −0/+0	0 −0/+0
Sulfate	6 −1/+2	7 −1/+2	8 −3/+7	7 −2/+4	8 −1/+3
Carbonate	1 −1/+0	3 −0/+0	1 −0/+0	2 −0/+0	3 −0/+0
Shocked feldspar	26 −4/+6	0 −0/+0	4 −4/+2	20 −5/+9	0 −0/+0
Modeled iron distribution, % Fe in					
Olivine	28 −0/+2	74 −1/+0	43 −13/+18	37 −25/+10	71−5/+2
Pyroxene	66 −2/+0	19 −2/+4	51 −28/+17	57 −9/+25	23 −4/+7
Magnetite	0 −0/+0	0 −0/+0	1 −1/+12	0 −0/+0	0 −0/+0
Hematite	0 −0/+0	0 −0/+0	0 −0/+0	0 −0/+0	0 −0/+0
Phyllosilicate	0 −0/+0	5 −3/+2	1 −1/+0	1 −1/+0	4 −2/+1
Amphibole	1 −1/+0	1 −1/+0	2 −1/+0	0 −0/+0	0 −0/+0
Carbonate	0 −0/+0	0 −0/+0	0 −0/+0	0 −0/+0	0 −0/+0
Plagioclase	6 −0/+0	1 −0/+0	1 −1/+0	4 −1/+2	1 −0/+1
olv/pyx	0 −0/+0	4 −1/+1	1 −0/+2	1 −1/+0	3 −1/+1
Chemistry (H_2O- and CO_2-free), wt %					
SiO_2	48 −1/+1	50 −5/+3	49 −7/+0	48 −1/+0	48 −0/+0
Al_20_3	12 −0/+0	14 −1/+1	11 −6/+0	12 −1/+2	13 −0/+1
FeO	14 −1/+2	10 −1/+0	15 −0/+6	14 −1/+0	12 −1/+0
MgO	8 −0/+0	8 −0/+0	9 −2/+4	9 −4/+3	10 −1/+1
CaO	12 −2/+0	13 −2/+3	10 −2/+2	10 −1/+2	10 −1/+1
Na_2O	2 −0/+0	1 −0/+0	1 −1/+0	1 −0/+0	1 −0/+0
MnO	0 −0/+0	0 −0/+0	0 −0/+0	0 −0/+0	0 −0/+0
K_2O	1 −0/+0	1 −0/+0	1 −0/+0	1 −0/+0	2 −0/+0
TiO_2	0 −0/+0	0 −0/+0	0 −0/+0	0 −0/+0	0 −0/+0
SO_3	3 −1/+1	4 −0/+1	4 −2/+3	3 −1/+2	4 −1/+1
H_2O (unnormalized)	1 −1/+0	2 −1/+0	2 −1/+0	2 −1/+0	2 −0/+0
CO_2 (unnormalized)	1 −0/+1	1 −0/+1	1 −0/+2	1 −0/+2	2 −0/+1

	No Olivine	No Plagioclase	No Sheet-sid	No Sulfate
Derived abundances, vol %				
Quartz	0 ± 0	0 ± 0	0 ± 0	1 ± 1
Alkali Feldspar	3 ± 2	7 ± 1	6 ± 1	9 ± 2
Plagioclase	30 ± 4	0 ± 0	17 ± 5	28 ± 4
Orthopyroxene	1 ± 3	4 ± 2	6 ± 4	8 ± 3
Pigeonite	12 ± 4	17 ± 4	15 ± 5	6 ± 4
High-Ca clinopyroxene	18 ± 3	4 ± 3	10 ± 3	8 ± 5
Olivine	0 ± 0	20 ± 1	14 ± 2	13 ± 3
Sheet-silicates	5 ± 3	2 ± 3	0 ± 0	9 ± 4
Opal and glasses	7 ± 7	25 ± 7	14 ± 7	12 ± 4
Amphibole	0 ± 0	4 ± 1	4 ± 2	2 ± 2
Oxides	0 ± 0	5 ± 2	2 ± 2	0 ± 0
Sulfate	10 ± 2	11 ± 1	10 ± 1	0 ± 0
Carbonate	3 ± 1	1 ± 1	2 ± 1	3 ± 1
Shocked feldspar	10 ± 5	0 ± 0	0 ± 0	0 ± 0
Derived abundances, wt %				
Quartz	0 −0/+0	0 −0/+0	0 −0/+0	0 −0/+0
Alkali Feldspar	3 −0/+0	6 −1/+2	5 −1/+2	8 −3/+16
Plagioclase	26 −8/+6	0 −0/+0	14 −5/+3	25 −21/+2
Orthopyroxene	2 −2/+1	5 −5/+3	7 −4/+4	10 −2/+0
Pigeonite	13 −3/+5	19 −3/+5	17 −4/+4	7 −1/+2
High-Ca clinopyroxene	21 −5/+9	4 −3/+1	11 −0/+0	9 −7/+6
Olivine	0 −0/+0	26 −1/+3	17 −5/+6	18 −1/+0
Sheet-silicates	4 −2/+0	1 −1/+2	0 −0/+0	7 −2/+8
Opal and glasses	6 −6/+5	17 −3/+2	11 −0/+3	10 −1/+3
Amphibole	0 −0/+0	5 −1/+1	4 −3/+2	2 −0/+0
Oxides	0 −0/+0	8 −1/+0	3 −3/+1	0 −0/+0
Sulfate	8 −1/+4	8 −2/+3	8 −2/+3	0 −0/+0
Carbonate	3 −0/+0	1 −0/+0	2 −0/+0	3 −1/+2
Shocked feldspar	16 −2/+0	0 −0/+0	0 −0/+0	0 −0/+0
Modeled iron distribution, % Fe in				
Olivine	0 −0/+0	42 −1/+4	40 −8/+13	61 −5/+7
Pyroxene	87 −2/+3	28 −1/+2	42 −0/+4	34 −7/+5
Magnetite	0 −0/+0	28 −6/+2	15 −15/+7	0 −0/+0
Hematite	0 −0/+0	0 −0/+0	0 −0/+0	0 −0/+0
Phyllosilicate	6 −1/+0	0 −0/+0	0 −0/+0	2 −1/+2

Table 4. (continued)

	No Olivine	No Plagioclase	No Sheet-sid	No Sulfate
Amphibole	0 −0/+0	1 −0/+0	2 −1/+1	1 −0/+0
Carbonate	0 −0/+0	0 −0/+0	0 −0/+0	0 −0/+0
Plagioclase	7 −2/+2	0 −0/+0	0 −0/+0	2 −1/+0
olv/pyx	0 −0/+0	1 −0/+0	1 −0/+0	2 −0/+1
Chemistry (H_2O- and CO_2-free), wt %				
SiO2	48 −4/+3	47 −2/+2	46 −1/+2	54 −1/+5
Al203	16 −3/+1	4 −1/+0	9 −2/+1	12 −2/+0
FeO	8 −1/+2	27 −2/+1	18 −1/+0	14 −1/+3
MgO	7 −1/+0	11 −1/+1	11 −1/+1	10 −3/+1
CaO	15 −2/+3	5 −1/+1	9 −0/+0	7 −4/+1
Na2O	2 −0/+0	0 −0/+0	1 −0/+0	1 −0/+0
MnO	1 −0/+0	0 −0/+0	0 −0/+0	0 −0/+0
K2O	1 −0/+0	1 −0/+0	1 −0/+0	1 −0/+2
TiO2	0 −0/+0	0 −0/+0	0 −0/+0	0 −0/+0
SO3	4 −0/+2	4 −1/+2	4 −1/+2	0 −0/+0
HO (unnormalized)	1 −0/+2	3 −2/+0	2 −1/+0	1 −0/+2
CO_2 (unnormalized)	1 −0/+2	0 −0/+3	1 −0/+1	1 −1/+0

are multiplied by the modeled weight fraction of that end-member and then combined to produce the derived "whole rock" chemical composition. The contribution of iron from each mineral group (i.e., iron in olivine, pyroxene, amphibole, carbonate, clay, magnetite and hematite) to the whole rock $FeO_{(Total)}$ percentage is also calculated.

[26] Chemical information measured using electron microprobe is available for most spectra in the library used in this work [*Christensen et al.*, 2000b]. Where chemical information was not available, the chemistry was approximated using the stoichiometric chemical formula of those minerals (five spectra, Table 2). Finally, spectra from two shocked anorthosite (90% bytownite (An_{75}), 10% pyroxene) samples [*Johnson et al.*, 2002] were included in the library, with corresponding shock pressures of ~23 and ~56 GPa (Table 2). Chemical information was not provided for these samples; however, *Johnson et al.* [2002] report that the sample was taken from the AN-II unit of the Stillwater Complex Middle Banded Series [*Haskin and Salpas*, 1992]. *Haskin and Salpas* [1992] published a whole rock chemical composition for a similar anorthosite sample from AN-II, consisting of 85–95% labradorite (An_{68}) and 10–15% pyroxene; that composition was used as an estimate for the shocked anorthosite samples of *Johnson et al.* [2002]. Finally, it is known that the density of plagioclase increases with increasing shock pressure [*Ahrens and Rosenberg*, 1966]. Using the specific volumes measured for plagioclase shocked under varying pressures [*Ahrens and Rosenberg*, 1966], we interpolated density values of 3.7 and 4.5 g cm^{-3}, for the anorthosite shock pressures of 23 and 56 GPa, respectively.

[27] As *Wyatt et al.* [2001] correctly pointed out, the accuracy of the chemistry derived from thermal emission spectra is dependent on the spectra available in the library. That aspect of the method can be used to our advantage to rule out incorrect end-members or phases. The average chemistry and iron distribution of low-sulfur, low-albedo soils measured with APXS and MB (Table 3) is used as the known chemistry and iron distribution of basaltic sands. Derived mineralogical composition from models where the associated chemical abundances and iron distributions do not agree with either of these target APXS and MB compositions within error are discarded from the set of possible mineralogical composition solutions.

4. Results

4.1. Sand Mineralogical Composition From Mini-TES, APXS, and MB Data

[28] Mineralogical composition, chemical composition and iron distribution derived from each model run are shown in Table 4. Phase group abundance errors shown in Table 4 are calculated as described in section 3.3. Chemical abundances and iron distributions are calculated for the phase abundances and for the range of possible phase abundances determined by their associated errors. The resulting range of chemical abundances and iron distributions define the errors shown for each value. Model fits for each library are shown in Figure 3, arranged in order of increasing RMS error. For libraries where sulfate, olivine, low-Ca pyroxene, high-silica phases (phyllosilicates, opal and glass), or plagioclase spectra are excluded, the degradation in overall fit is most noticeable (based on visual inspection and higher RMS errors), providing a first indicator that each of these mineral groups are significant.

[29] Models using the full library as well as those that exclude high-silica phases, alkali feldspar, high-Ca pyroxene, orthopyroxene and amphibole, are possible matches to the MB measurements (Figure 4). As mentioned above, models which exclude sulfate, all low-Ca pyroxene, or plagioclase produce noticeably worsened fits to the Mini-TES spectrum; similarly, these models produce calculated Fe distributions that are much richer or poorer in olivine than the MB measurements (Figure 4). The model which excludes pigeonite also yields high iron proportions in olivine (Figure 4); however, in this case, the overall spectral fit is not adversely affected (Figure 3). This is an example of where the resulting change in chemical composition and iron distribution is especially useful in evaluating whether a derived mineralogical composition is acceptable. Finally, models which exclude carbonate or sheet silicates produce subequal proportions of iron in olivine and pyroxene, but these models also predict an excessive amount of iron

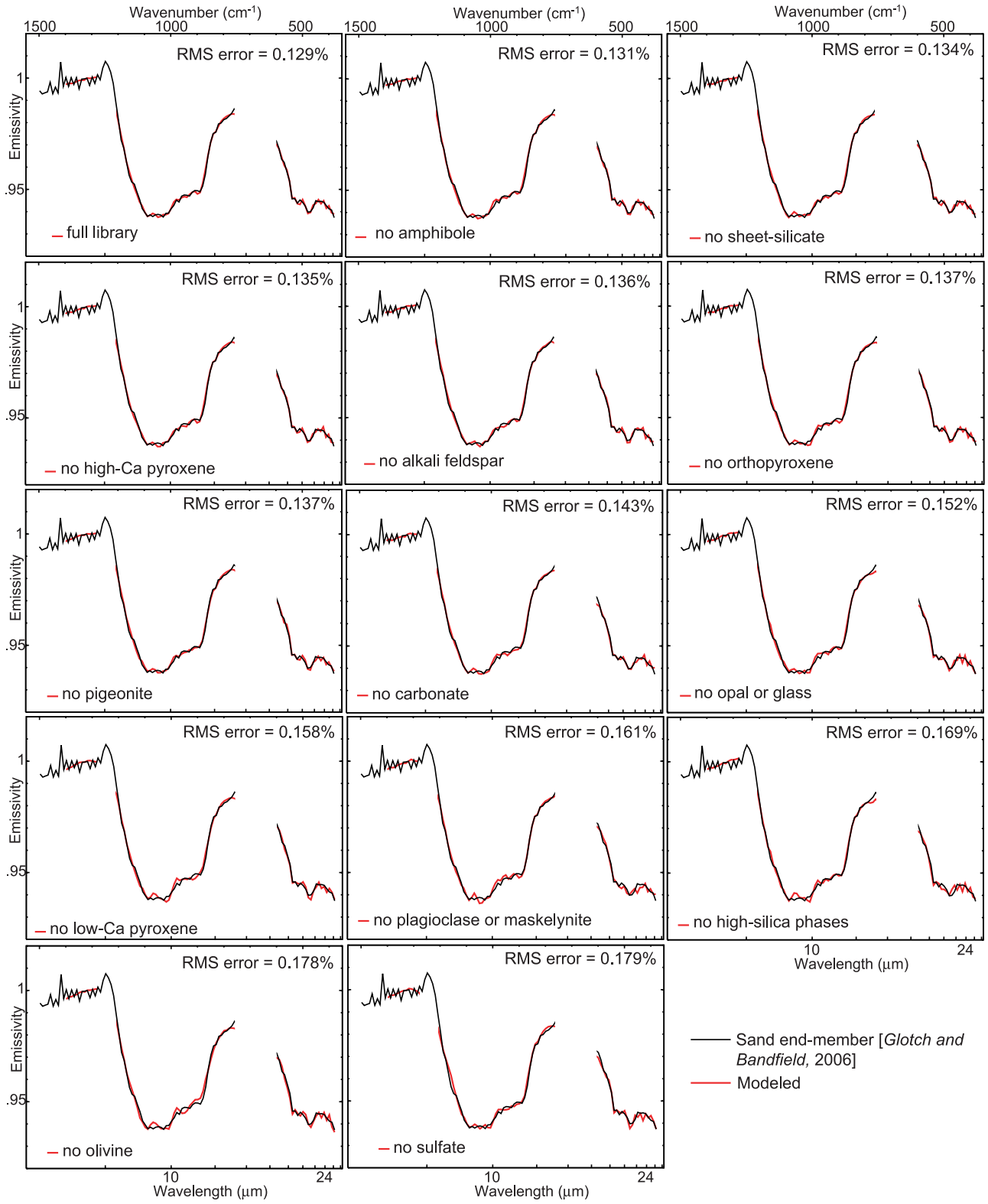

Figure 3. Model fits from each library, in order of increasing RMS error. Spectral fitting was constrained to the following wavelengths: 379–1210 cm^{-1} and 1270–1400 cm^{-1}. The 1210–1270 cm^{-1} portion of the Mini-TES basaltic sands end-member was excluded from modeling because it contains emissivity values greater than 1.0.

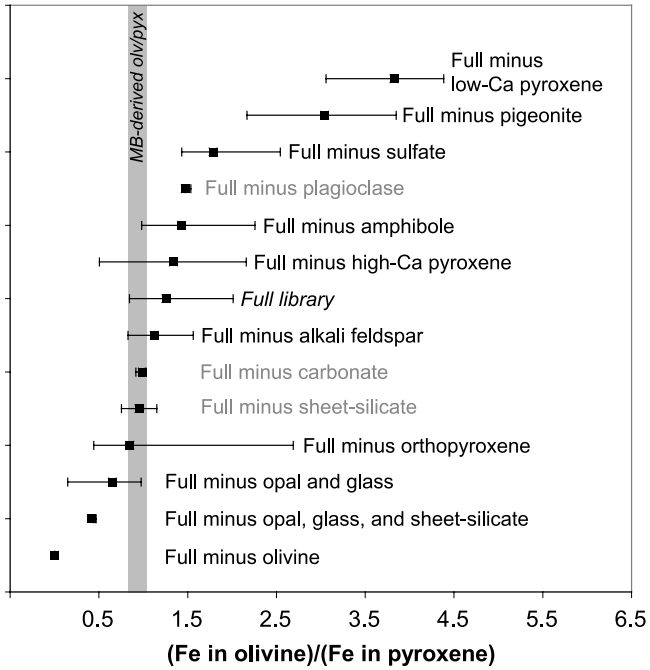

Figure 4. Mini-TES derived proportions of iron in olivine and pyroxene. The pyroxene and olivine iron distribution of low-sulfur soils determined by MB [*Morris et al.*, 2006] is shown for comparison. Models that exclude carbonate, plagioclase, and sheet silicates (gray text in figure) yield more than 15% of iron distributed in magnetite, which is inconsistent with MB measurements [*Morris et al.*, 2006]. Errors on Mini-TES derived phases are calculated using the method described in section 3.3.1.

distributed in magnetite compared to the MB measurements (Table 4).

[30] Figure 5 shows plots of derived SiO_2, Al_2O_3, MgO, FeO, CaO and SO_3 for the models which most closely matched the MB iron distributions (described above), versus the average composition of low-sulfur soils measured by APXS (Table 3). None of these models match all of the major oxide abundances within uncertainties of both instruments. One possible cause for the mismatch is that the APXS measurements of undisturbed low-sulfur soils may have contained a small fraction of fine-particulate dust, whereas the Mini-TES spectrum of dark sands was mathematically separated from spectral contributions of dust (section 3.2.1). Mini-TES-derived FeO and SO_3 abundances are usually lower than that of the APXS average low-sulfur soil, while CaO, MgO, Al_2O_3 and SiO_2 are usually higher. To test the suggestion that dust contamination could be causing the discrepancy, we added the Mini-TES derived compositions for these six models in varying proportions to the chemical composition of the soil target "MontBlanc_LesHauches" [*Morris et al.*, 2006]. This target has the highest proportion of nanophase oxide observed with Opportunity and is the target most representative of Martian dust [*Morris et al.*, 2006]. Even with addition of up to 40 wt % dust, not all of the major oxides can be matched to within the uncertainty of both instruments (Figure 6). However, it is apparent that the addition of dust does bring all major oxides closer to the APXS values, suggesting that dust is likely the major reason for the discrepancy. Other potential causes for the mismatch between Mini-TES and APXS-determined chemistry are that (1) some contamination of spherules was also present in the APXS measurement of undisturbed low-sulfur soils, (2) one or more true compositional end-members are missing from the spectral library used in this study, (3) the Mini-TES sand end-member was derived from many different surface targets [*Glotch and Bandfield*, 2006], whereas the APXS dark sand composition is an average of only five targets, and/or (4) the abundances of end-members are slightly inaccurate due to variations in particle size between library samples.

[31] Though there is slight disagreement between the Mini-TES-derived compositions and APXS measurements, we present the best fit mineralogical composition in Table 1. This composition is simply the average of model results for the six libraries that best matched the MB-derived iron distribution, discussed above. Plagioclase, pigeonite, olivine, high-silica phases and sulfate are modeled at abundances well above the ~5–10% detection limit. This best fit composition is discussed in section 5.

4.2. Comparison of Mini-TES and TES Data

[32] At the spatial sampling of the TES instrument (~3 × 8 km per pixel), a single TES spectrum is likely sampling all of the major surface components observed by Opportunity (dust, outcrop, hematite and basalt). It is impossible to resolve hematite-free surfaces within Meridiani Planum at that scale; however, the contribution from the other major surface components, outcrop and dust, may be minimized by selecting spectra from the lowest-albedo surfaces within Meridiani Planum. For comparison to the Mini-TES derived basaltic shape and composition, only TES spectra from the darkest surfaces within Meridiani Planum were used. Ideally, only spectra that sample the Opportunity landing site would be analyzed; however, the large pixel size of the TES instrument precludes that option. Instead, an expanded selection region must be used in order to achieve adequate signal to noise. The following constraints were used to retrieve > 120 high-quality spectra from five orbits within the area 1.9–2.7°S, 2.1–5.0°W: MGS mapping phase orbit numbers between 1 and 5317, target temperatures > 255 K, total dust extinction < 0.15, total water ice extinction < 0.04, emission angles < 30°, and TES lambert albedo values ≤ 0.12. Spectra within those constraints were averaged within each orbit and converted to surface emissivity using the least squares fitting method described in section 3.2 and by *Smith et al.* [2000]. Spectral samples between 260 and 508 cm^{-1} and 825–1301 cm^{-1} were used for surface-atmosphere separation. For direct comparison to the Mini-TES basaltic sand end-member, the hematite contribution was removed from the TES spectrum by scaling the hematite end-member in proportion to its modeled abundance and subtracting it.

[33] Figure 7 shows a comparison of the Mini-TES basaltic sand end-member [*Glotch and Bandfield*, 2006] and the TES-derived surface emissivity shape from this study. The difference in the wavelength position of the maximum emissivity is likely due to minor CO_2 isotope absorptions present in TES data. The positions of these

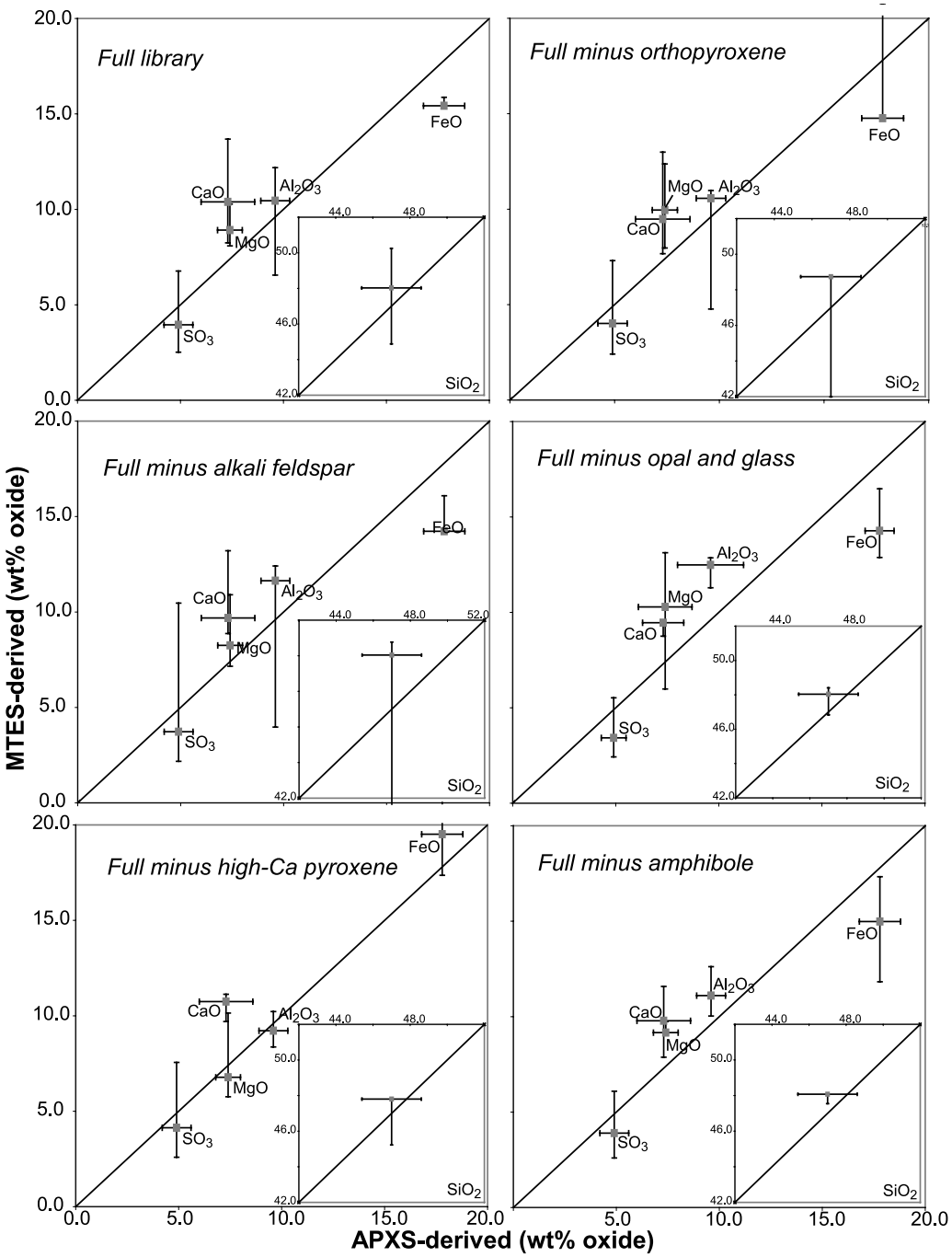

Figure 5. Mini-TES derived major oxide abundances compared with APXS-measured abundances for the six models which matched MB-derived iron distributions in olivine and pyroxene.

absorptions overlap with the Christiansen frequency of basaltic materials. In the conversion of radiance to apparent emissivity (following the method of *Christensen* [1998]), the wavelength with the highest brightness temperature is typically just below that of the CO_2 isotope band, thereby placing the position of maximum apparent emissivity at slightly higher wave numbers than typical for basaltic materials. Finally, the mismatch between the Mini-TES end-member and the TES-derived emissivity (minus hematite contribution) in the $\sim$1070–1200 cm^{-1} spectral region (Figure 7) is likely due to minor overcorrection for atmospheric dust.

[34] Derived mineral abundances from the average surface emissivity spectrum are shown in Table 1. Though only results from the MNN model are shown in Table 1, we note here that derived phase abundances were within 5% of those from the ILR model. The surface dust spectrum of *Bandfield and Smith* [2003], though included in the library, was not used by either model. Once normalized for $\sim$20% hematite abundance, the remaining derived mineral abundances are

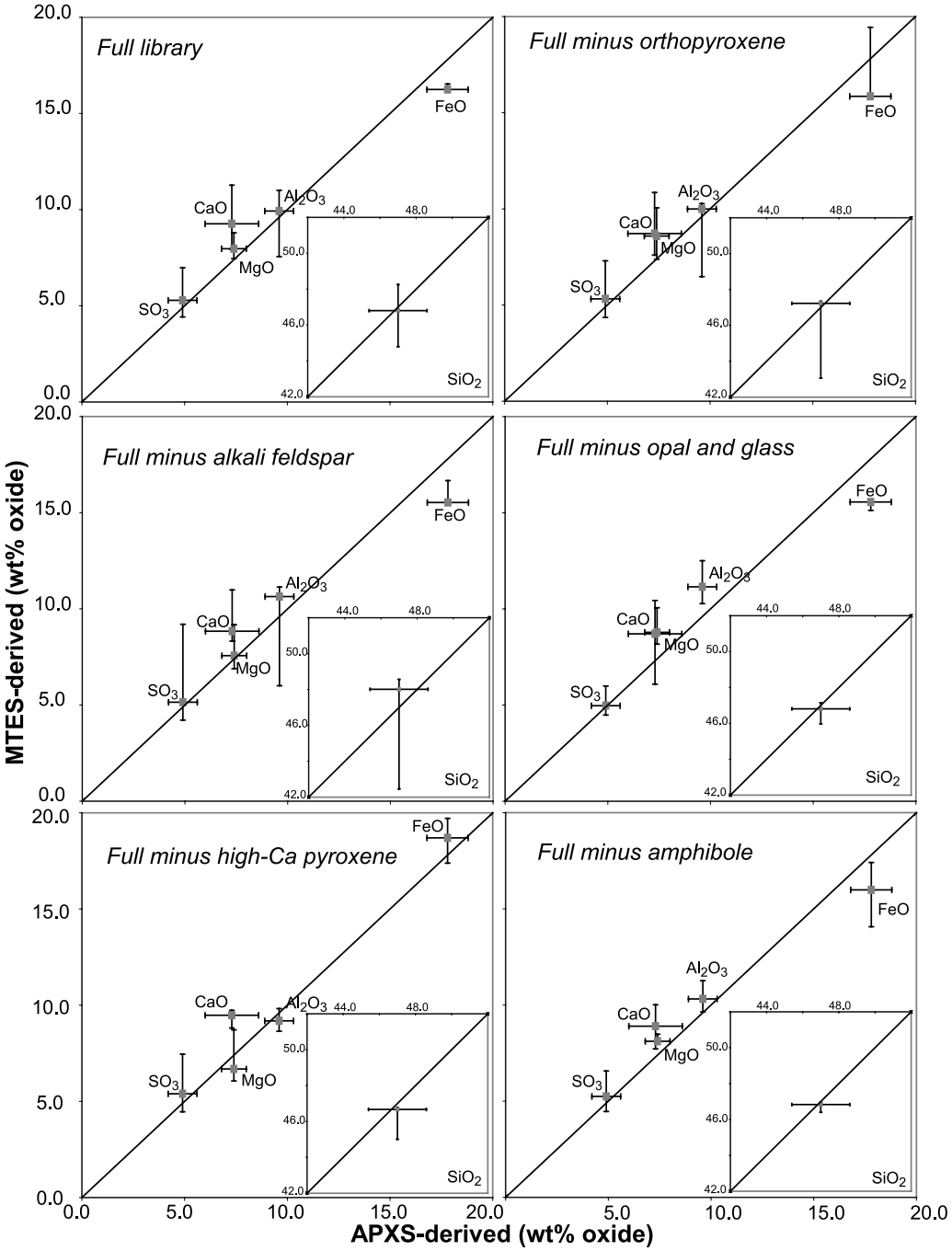

Figure 6. Mini-TES derived major oxide abundances shown in Figure 5, with the addition of 40% Meridiani Planum dust [*Morris et al.*, 2006]. See text for explanation. Data points are calculated by 0.60(MTES) + 0.40(MP dust).

within 5% of the Mini-TES derived abundance (Table 1). In general, all discrepancies are within the statistical error for phases derived from the TES spectrum (Table 1).

5. Discussion

[35] The mineralogical composition derived in this study indicates that the sand component of Meridiani Planum consists of olivine basalt plus a small amount of amorphous silica (either primary or secondary in origin) and sulfate (Table 1). While this composition is broadly consistent with those predicted from unconstrained models in previous studies [*Yen et al.*, 2005; *Glotch and Bandfield*, 2006], the methods of this study allow for more precise determination of pyroxene composition and absolute abundances of all phases. Better constraints on mineralogical composition are important for studies of mechanical and chemical weathering of Martian soils and rocks, as well as for comparison to Martian meteorite and local rock compositions measured by

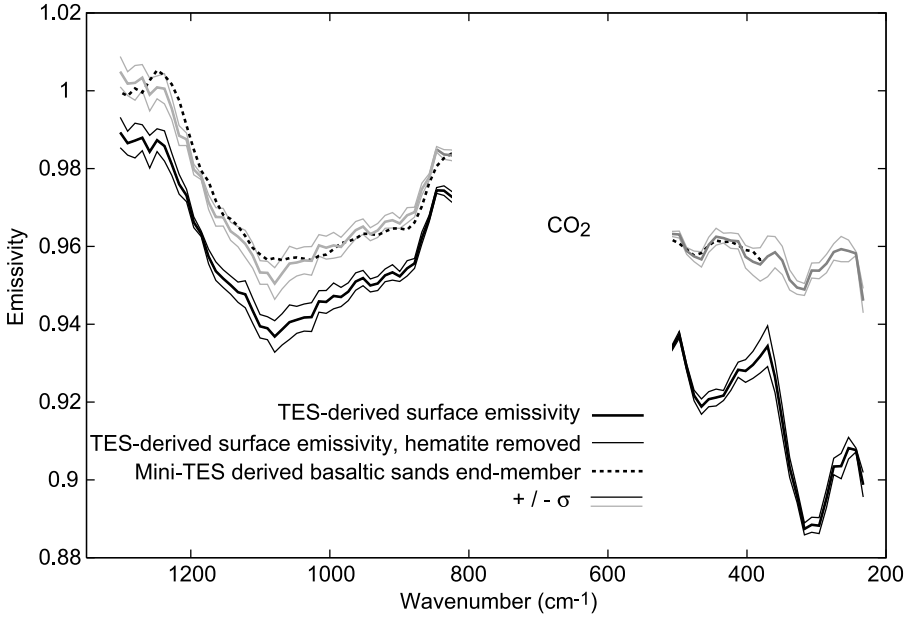

Figure 7. TES-derived surface emissivity of Meridiani Planum low-albedo surfaces, TES-derived surface emissivity minus hematite contribution, and Mini-TES derived basaltic sand end-member [*Glotch and Bandfield*, 2006].

MER. An estimate of the uncertainty associated with individual abundances is also presented.

[36] Results from this study suggest that the basaltic sands contain ~10 vol % sulfate (~8% by weight). This sulfate is not due to admixture of bright dust (which also contains sulfate [e.g., *Yen et al.*, 2005]) but rather is a mathematically inseparable component of the coarse particulate sand (section 3.2.1). The fit to the Mini-TES spectrum noticeably worsens when sulfate is excluded from the library (Figure 3), and excluding sulfate causes the Mini-TES derived iron distribution to be more heavily weighted in olivine (Figure 4). The APXS measured an appreciable amount of sulfur in both bright and dark soils [*Rieder et al.*, 2004]. Sulfur concentration is higher in the bright dust relative to dark soils; however, there is no corresponding increase in other elements [*Yen et al.*, 2005]. The lack of evidence for a sulfate cation led *Yen et al.* [2005] to suggest that the sulfur may have been originally deposited as H_2SO_4, a likely precipitate of volcanic outgassing [*Clark and Baird*, 1979]. That sulfur then formed localized sulfates on existing soil grains, resulting in a nondistinct sulfate composition in the sand and dust. Because of the relatively low abundance and spectral similarity of sulfate species used in this study, it is difficult to confirm this suggestion through modeling of Mini-TES spectra. However, the results from this work are consistent with this scenario. Alternative explanations for the sulfate in the dark sands may be that it was derived from the local outcrop [*Yen et al.*, 2005], or may have been transported from a more distant source.

[37] The pyroxene composition suggested from this study is also of interest. Figure 4 indicates that without the inclusion of pigeonite (in this work, an iron-rich sample), the Mini-TES derived iron distribution is heavily weighted toward olivine. Pigeonite has been modeled at or near the traditional detection limits in previous TES analyses of Martian dark regions [e.g., *Rogers and Christensen*, 2007]; however, there has been no definitive evidence of its existence from orbital observations alone. Spectral features attributable to pigeonite have been identified with Mini-TES in some Gusev rocks [*Ruff et al.*, 2006] as well as in "Bounce Rock," a likely piece of impact ejecta analyzed by Opportunity on the Meridiani Plains [*Christensen et al.*, 2004; *Klingelhöfer et al.*, 2004]. Results from this study strongly argue that pigeonite, or at least an iron-rich pyroxene, is a required component of Meridiani Planum surface materials. At the time of writing, only one pigeonite spectrum, taken from a synthetic sample [*Hamilton*, 2000], is available for analysis. Models that use additional low-Ca clinopyroxene compositional ranges may help to support or refute this result. If pigeonite is the only pyroxene included in the spectral library, the resulting iron distribution derived from deconvolution of Mini-TES data predicts ~35% Fe in magnetite, which is inconsistent with MB observations. Thus although pigeonite is the only pyroxene modeled well above the detection limit, it is clear that either orthopyroxene or high-Ca pyroxene is needed in addition to pigeonite in order to achieve an iron distribution that is consistent with MB measurements.

[38] The volume abundance of olivine in the dark sands ranges between ~10–15%. Although the proportion of iron in olivine is approximately equal to that in pyroxene [*Morris et al.*, 2006], the volume abundance of pyroxene is twice the volume abundance of olivine. This may partially explain why olivine is less readily detected than pyroxene in OMEGA spectra of the Meridiani Plains [*Arvidson et al.*, 2006].

[39] The basaltic sand composition derived from combined Mini-TES, APXS, and MB data is consistent with that derived from TES data of Meridiani Planum low-albedo surfaces. We note that the full library gave one of the best matches to the MB mineralogical composition, which

provides evidence of the overall accuracy of TES deconvolutions even where supporting compositional information is not available. Results from this study support the accuracy of global-scale variations in mineralogical composition observed previously [e.g., *Rogers and Christensen*, 2007] and validate TES derived mineral abundances elsewhere on Mars.

[40] The Meridiani Planum sand composition derived from this study is very similar to that derived for the majority of the highlands with TES data ("compositional group 3" of *Rogers and Christensen* [2007]). In addition, preliminary analyses of small bedrock exposures in the northern Noachis Terra region of Mars indicate similar compositions to the more widespread sand deposits of the highlands (compositional group 3) and to Meridiani Planum sands [e.g., *Rogers et al.*, 2007]. It is possible that bedrock exposures such as these are the source for Meridiani Planum sands.

[41] The compositions and abundances of minerals present in the dark regions of Meridiani Planum suggest a relatively unaltered olivine basaltic composition, with minor amounts of sulfate and primary or secondary amorphous silica. This composition is consistent with conclusions from previous studies of Martian dark regions conducted with orbital measurements: that surface materials have likely undergone, at most, minor aqueous alteration relative to surfaces on Earth, implying limited interaction with liquid water [e.g., *Soderblom*, 1992; *Christensen et al.*, 2000a; *Bandfield*, 2002; *Bibring et al.*, 2005; *Rogers and Christensen*, 2007].

6. Conclusions

[42] From our results we conclude the following:

[43] 1. Dark sands on the plains of Meridiani Planum are olivine basaltic in composition, consistent with previous estimates. The sands contain only minor amounts of aqueous alteration products, implying limited interaction with liquid water.

[44] 2. Iron-rich pigeonite or another iron-rich pyroxene, and sulfate are likely components of the sand. These have been suggested previously from orbital measurements of Martian dark regions; however, the detections were equivocal. Results from this study strongly indicate their existence in Meridiani Planum low-albedo materials.

[45] 3. The volume abundance of olivine (~10–15%) is approximately half that of pyroxene; this is consistent with the subequal proportions of iron in olivine and pyroxene indicated by MB data.

[46] 4. The basaltic sand composition derived from Mini-TES, APXS, and MB data is consistent with that derived from TES data of Meridiani Planum low-albedo surfaces. These results demonstrate the accuracy of TES-derived mineralogical information and support observations of global- and regional-scale variations in mineralogical composition presented in previous studies using TES data [e.g., *Bandfield*, 2002; *Rogers and Christensen*, 2007].

[47] 5. The analysis presented in section 3 demonstrates that the MNN least squares method is generally more reliable than the ILR method and will be a useful technique in future TES and Mini-TES spectral analyses. The examples given in this study demonstrate the value of using library-preserving optimization methods to derive mineralogical compositions [e.g., *Seelos and Arvidson*, 2003; *Staid et al.*, 2004; *Johnson et al.*, 2006; *Noe Dobrea et al.*, 2006].

[48] **Acknowledgments.** We are grateful for discussions and comments provided by Jeffrey Johnson, Albert Yen, and Timothy Glotch. Kimberly Murray (née Feely) graciously provided the rock spectra and petrographic abundances from *Feely and Christensen* [1999]. Formal reviews from Steven Ruff and Karen Stockstill-Cahill greatly improved and clarified this manuscript. We appreciate the outstanding efforts of the scientists and engineers involved in development and operation of the MER mission and Mini-TES instruments. This work was partially supported by the NASA Mars Data Analysis Program (grant NNX06AD94G) and the Mars Exploration Rover Participating Scientist program.

References

Ahrens, T. J., and J. T. Rosenberg (1966), Shock metamorphism: Experiments on quartz and plagioclase, in *Shock Metamorphism of Natural Materials*, edited by B. M. French and N. M. Short, pp. 59–81, Mono Book, Baltimore, Md.

Arvidson, R. E., F. P. Seelos IV, K. S. Deal, W. C. Koeppen, N. O. Snider, J. M. Kieniewicz, B. M. Hynek, M. T. Mellon, and J. B. Garvin (2003), Mantled and exhumed terrains in Terra Meridiani, Mars, *J. Geophys. Res.*, *108*(E12), 8073, doi:10.1029/2002JE001982.

Arvidson, R. E., F. Poulet, J. P. Bibring, M. Wolff, A. Gendrin, R. V. Morris, J. J. Freeman, Y. Langevin, N. Mangold, and G. Bellucci (2005), Spectral Reflectance and Morphologic Correlations in Eastern Terra Meridiani, Mars, *Science*, *307*, 1591–1594, doi:10.1126/science.1109509.

Arvidson, R. E., et al. (2006), Nature and origin of the hematite-bearing plains of Terra Meridiani based on analyses of orbital and Mars Exploration rover data sets, *J. Geophys. Res.*, *111*, E12S08, doi:10.1029/2006JE002728.

Baldridge, A. M., and W. M. Calvin (2004), Hydration state of the Martian coarse-grained hematite exposures: Implications for their origin and evolution, *J. Geophys. Res.*, *109*, E04S90, doi:10.1029/2003JE002066.

Bandfield, J. L. (2002), Global mineral distributions on Mars, *J. Geophys. Res.*, *107*(E6), 5042, doi:10.1029/2001JE001510.

Bandfield, J. L., and M. D. Smith (2003), Multiple emission angle surface-atmosphere separations of Thermal Emission Spectrometer data, *Icarus*, *161*(1), 47–65, doi:10.1016/S0019-1035(02)00025-8.

Bandfield, J. L., P. R. Christensen, and M. D. Smith (2000a), Spectral data set factor analysis and end-member recovery: Application to analysis of Martian atmospheric particulates, *J. Geophys. Res.*, *105*(E4), 9573–9587, doi:10.1029/1999JE001094.

Bandfield, J. L., V. E. Hamilton, and P. R. Christensen (2000b), A global view of Martian surface compositions from MGS-TES, *Science*, *287*(5458), 1626–1630, doi:10.1126/science.287.5458.1626.

Bell, J. F., III, et al. (2003), Mars Exploration Rover Athena Panoramic Camera (Pancam) investigation, *J. Geophys. Res.*, *108*(E12), 8063, doi:10.1029/2003JE002070.

Bell, J. F., et al. (2004), Pancam multispectral imaging results from the Opportunity Rover at Meridiani Planum, *Science*, *306*(5702), 1703–1709, doi:10.1126/science.1105245.

Bell, J. F., III, M. S. Rice, J. R. Johnson, and T. M. Hare (2008), Surface albedo observations at Gusev Crater and Meridiani Planum, Mars, *J. Geophys. Res.*, doi:10.1029/2007JE002976, in press.

Bevington, P. R., and D. K. Robinson (2003), *Data Reduction and Error Analysis for the Physical Sciences*, 320 pp., McGraw-Hill, New York.

Bibring, J. P., et al. (2005), Mars surface diversity as revealed by the OMEGA/Mars Express observations, *Science*, *307*(5715), 1576–1581, doi:10.1126/science.1108806.

Christensen, P. R. (1998), Variations in Martian surface composition and cloud occurrence determined from thermal infrared spectroscopy: Analysis of Viking and Mariner 9 data, *J. Geophys. Res.*, *103*(E1), 1733–1746, doi:10.1029/97JE02114.

Christensen, P. R., J. L. Bandfield, V. E. Hamilton, D. A. Howard, M. D. Lane, J. L. Piatek, S. W. Ruff, and W. L. Stefanov (2000a), A thermal emission spectral library of rock-forming minerals, *J. Geophys. Res.*, *105*(E4), 9735–9739, doi:10.1029/1998JE000624.

Christensen, P. R., J. L. Bandfield, M. D. Smith, V. E. Hamilton, and R. N. Clark (2000b), Identification of a basaltic component on the Martian surface from Thermal Emission Spectrometer data, *J. Geophys. Res.*, *105*(E4), 9609–9621, doi:10.1029/1999JE001127.

Christensen, P. R., et al. (2001), Mars Global Surveyor Thermal Emission Spectrometer experiment: Investigation description and surface science results, *J. Geophys. Res.*, *106*(E10), 23,823–23,871, doi:10.1029/2000JE001370.

Christensen, P. R., et al. (2003), Miniature Thermal Emission Spectrometer for the Mars Exploration Rovers, *J. Geophys. Res.*, *108*(E12), 8064, doi:10.1029/2003JE002117.

Christensen, P. R., et al. (2004), Mineralogy at Meridiani Planum from the Mini-TES experiment on the Opportunity Rover, *Science*, *306*(5702), 1733–1739, doi:10.1126/science.1104909.

Clark, B. C., and A. K. Baird (1979), Is the Martian lithosphere sulfur rich?, *J. Geophys. Res.*, *84*(B14), 8395–8403, doi:10.1029/JB084iB14p08395.

Conel, J. E. (1969), Infrared emissivities of silicates: Experimental results and a cloudy atmosphere model of spectral emission from condensed particulate mediums, *J. Geophys. Res.*, *74*(6), 1614–1634, doi:10.1029/JB074i006p01614.

Feely, K. C., and P. R. Christensen (1999), Quantitative compositional analysis using thermal emission spectroscopy: Application to igneous and metamorphic rocks, *J. Geophys. Res.*, *104*(E10), 24,195–24,210, doi:10.1029/1999JE001034.

Gendrin, A., et al. (2005), Sulfates in Martian layered terrains: The OMEGA/Mars Express view, *Science*, *307*(5715), 1587–1591, doi:10.1126/science.1109087.

Glotch, T. D., and J. L. Bandfield (2006), Determination and interpretation of surface and atmospheric Miniature Thermal Emission Spectrometer spectral end-members at the Meridiani Planum landing site, *J. Geophys. Res.*, *111*, E12S06, doi:10.1029/2005JE002671.

Glotch, T. D., R. V. Morris, P. R. Christensen, and T. G. Sharp (2004), Effect of precursor mineralogy on the thermal infrared emission spectra of hematite: Application to Martian hematite mineralization, *J. Geophys. Res.*, *109*, E07003, doi:10.1029/2003JE002224.

Hamilton, V. E. (2000), Thermal infrared spectroscopy of the pyroxene mineral series, *J. Geophys. Res.*, *105*(E4), 9701–9716.

Hamilton, V. E., and P. R. Christensen (2000), Determining the modal mineralogy of mafic and ultramafic igneous rocks using thermal emission spectroscopy, *J. Geophys. Res.*, *105*(E4), 9717–9733, doi:10.1029/1999JE001113.

Hamilton, V. E., M. B. Wyatt, H. Y. McSween, and P. R. Christensen (2001), Analysis of terrestrial and Martian volcanic compositions using thermal emission spectroscopy: 2. Application to Martian surface spectra from the Mars Global Surveyor Thermal Emission Spectrometer, *J. Geophys. Res.*, *106*(E7), 14,733–14,746, doi:10.1029/2000JE001353.

Haskin, L. A., and P. A. Salpas (1992), Genesis of compositional characteristics of Stillwater AN-I and AN-Ii thick anorthosite units, *Geochim. Cosmochim. Acta*, *56*(3), 1187–1212, doi:10.1016/0016-7037(92)90056-O.

Johnson, J. R., F. Horz, P. G. Lucey, and P. R. Christensen (2002), Thermal infrared spectroscopy of experimentally shocked anorthosite and pyroxenite: Implications for remote sensing of Mars, *J. Geophys. Res.*, *107*(E10), 5073, doi:10.1029/2001JE001517.

Johnson, J. R., M. I. Staid, T. N. Titus, and K. Becker (2006), Shocked plagioclase signatures in Thermal Emission Spectrometer data of Mars, *Icarus*, *180*, 60–74, doi:10.1016/j.icarus.2005.08.010.

Klingelhöfer, G., et al. (2002), The miniaturized Mossbauer spectrometer MIMOS II for extraterrestrial and outdoor terrestrial applications: A status report, *Hyperfine Interact.*, *144–145*(1–4), 371–379, doi:10.1023/A:1025444209059.

Klingelhöfer, G., et al. (2003), Athena MIMOS II Mössbauer spectrometer investigation, *J. Geophys. Res.*, *108*(E12), 8067, doi:10.1029/2003JE002138.

Klingelhöfer, G., et al. (2004), Jarosite and hematite at Meridiani Planum from Opportunity's Mossbauer spectrometer, *Science*, *306*(5702), 1740–1745, doi:10.1126/science.1104653.

Lawson, C. L., and R. J. Hanson (1974), *Solving Least-Squares Problems*, 340 pp., Prentice-Hall, Englewood Cliffs, N. J.

Lyon, R. J. P. (1965), Analysis of rocks by spectral infrared emission (8 to 25 μm), *Econ. Geol.*, *60*, 715–736.

Malinowski, E. R. (1991), *Factor Analysis in Chemistry*, 2nd ed., John Wiley, New York.

McSween, H. Y., Jr., T. L. Grove, and M. B. Wyatt (2003), Constraints on the composition and petrogenesis of the Martian crust, *J. Geophys. Res.*, *108*(E12), 5135, doi:10.1029/2003JE002175.

Meyer, E. F. (1997), A note on covariance in propagation of uncertainty, *J. Chem. Educ.*, *74*(11), 1339–1340.

Michalski, J. R., M. D. Kraft, T. Diedrich, T. G. Sharp, and P. R. Christensen (2003), Thermal emission spectroscopy of the silica polymorphs and considerations for remote sensing of Mars, *Geophys. Res. Lett.*, *30*(19), 2008, doi:10.1029/2003GL018354.

Michalski, J. R., M. D. Kraft, T. G. Sharp, L. B. Williams, and P. R. Christensen (2005), Mineralogical constraints on the high-silica Martian surface component observed by TES, *Icarus*, *174*(1), 161–177.

Michalski, J. R., M. D. Kraft, T. G. Sharp, L. B. Williams, P. R. Christensen, J. R. Emission Michalski, M. D. Kraft, T. G. Sharp, L. B. Williams, and P. R. Christensen (2006), Emission spectroscopy of clay minerals and evidence for poorly crystalline aluminosilicates on Mars from Thermal Emission Spectrometer data, *J. Geophys. Res.*, *111*, E03004, doi:10.1029/2005JE002438.

Milliken, R. E., J. F. Mustard, F. Poulet, D. Jouglet, J.-P. Bibring, B. Gondet, and Y. Langevin (2007), Hydration state of the Martian surface as seen by Mars Express OMEGA: 2. H_2O content of the surface, *J. Geophys. Res.*, *112*, E08S07, doi:10.1029/2006JE002853.

Morris, R. V., et al. (2006), Mössbauer mineralogy of rock, soil, and dust at Meridiani Planum, Mars: Opportunity's journey across sulfate-rich outcrop, basaltic sand and dust, and hematite lag deposits, *J. Geophys. Res.*, *111*, E12S15, doi:10.1029/2006JE002791.

Morse, S. A. (1996), Kiglapait mineralogy. 3. Olivine compositions and Rayleigh fractionation models, *J. Petrol.*, *37*(5), 1037–1061.

Murchie, S., L. Kirkland, S. Erard, J. Mustard, and M. Robinson (2000), Near-infrared spectral variations of Martian surface materials from ISM imaging spectrometer data, *Icarus*, *147*(2), 444–471, doi:10.1006/icar.2000.6446.

Mustard, J. F., S. Murchie, S. Erard, and J. Sunshine (1997), In situ compositions of Martian volcanics: Implications for the mantle, *J. Geophys. Res.*, *102*(E11), 25,605–25,615, doi:10.1029/97JE02354.

Mustard, J. F., F. Poulet, A. Gendrin, J. P. Bibring, Y. Langevin, B. Gondet, N. Mangold, G. Bellucci, and F. Altieri (2005), Olivine and pyroxene diversity in the crust of Mars, *Science*, *307*(5715), 1594–1597, doi:10.1126/science.1109098.

Noe Dobrea, E. Z., J. F. Bell, T. H. McConnochie, and M. Malin (2006), Analysis of a spectrally unique deposit in the dissected Noachian terrain of Mars, *J. Geophys. Res.*, *111*(E6), E06007, doi:10.1029/2005JE002431.

Ramsey, M. S., and P. R. Christensen (1998), Mineral abundance determination: Quantitative deconvolution of thermal emission spectra, *J. Geophys. Res.*, *103*(B1), 577–596, doi:10.1029/97JB02784.

Rieder, R., R. Gellert, J. Brückner, G. Klingelhöfer, G. Dreibus, A. Yen, and S. W. Squyres (2003), The new Athena alpha particle X–ray spectrometer for the Mars Exploration Rovers, *J. Geophys. Res.*, *108*(E12), 8066, doi:10.1029/2003JE002150.

Rieder, R., et al. (2004), Chemistry of rocks and soils at Meridiani Planum from the alpha particle X–ray spectrometer, *Science*, *306*(5702), 1746–1749, doi:10.1126/science.1104358.

Rogers, A. D., and P. R. Christensen (2007), Surface mineralogy of Martian low-albedo regions from MGS-TES data: Implications for upper crustal evolution and surface alteration, *J. Geophys. Res.*, *112*, E01003, doi:10.1029/2006JE002727.

Rogers, A. D., O. Aharonson, J. L. Bandfield, and P. R. Christensen (2007), The nature and origin of Mars' intercrater plains: New insight from THEMIS, *Lunar Planet. Sci.*, *XXXVIII*, Abstract 2313.

Ruff, S. W., P. R. Christensen, D. L. Blaney, W. H. Farrand, J. R. Johnson, J. R. Michalski, J. E. Moersch, S. P. Wright, and S. W. Squyres (2006), The rocks of Gusev Crater as viewed by the Mini-TES instrument, *J. Geophys. Res.*, *111*, E12S18, doi:10.1029/2006JE002747.

Seelos, F. P. I., and R. E. Arvidson (2003), Bounded variable least-squares-application of a constrained optimization algorithm to the analysis of TES emissivity spectra, *Lunar Planet. Sci.*, *XXXIV*, Abstract 1817.

Smith, M. D., J. L. Bandfield, and P. R. Christensen (2000), Separation of atmospheric and surface spectral features in Mars Global Surveyor Thermal Emission Spectrometer (TES) spectra, *J. Geophys. Res.*, *105*(E4), 9589–9607, doi:10.1029/1999JE001105.

Soderblom, L. A. (1992), The composition and mineralogy of the Martian surface from spectroscopic observations: 0.3 μm to 50 μm, in Mars, edited by H. H. Kieffer, B. Jakosky, C. W. Snyder, and M. S. Matthews. pp. 557–593, Univ. of Ariz., Tucson.

Squyres, S. W., et al. (2003), Athena Mars rover science investigation, *J. Geophys. Res.*, *108*(E12), 8062, doi:10.1029/2003JE002121.

Staid, M. I., J. R. Johnson, and L. R. Gaddis (2004), Analysis of Mars Thermal Emission Spectrometer data using large mineral reference libraries, *Lunar Planet. Sci. Conf.*, *XXXV*, Abstract 1778.

Wiseman, S. M. (2006), Photometric analysis of olivine and pyroxene using Hapke modeling, *Eos Trans. AGU*, *87*(52), Fall Meet. Suppl, Abstract P23C-0077.

Wyatt, M. B., V. E. Hamilton, H. Y. McSween, P. R. Christensen, and L. A. Taylor (2001), Analysis of terrestrial and Martian volcanic compositions using thermal emission spectroscopy: 1. Determination of mineralogy, chemistry, and classification strategies, *J. Geophys. Res.*, *106*(E7), 14,711–14,732, doi:10.1029/2000JE001356.

Yen, A. S., et al. (2005), An integrated view of the chemistry and mineralogy of Martian soils, *Nature*, *436*(7047), 49–54, doi:10.1038/nature03637.

O. Aharonson, Division of Geological and Planetary Sciences, California Institute of Technology, MC 150-21, Pasadena, CA 91125, USA.

A. D. Rogers, Department of Geosciences, State University of New York at Stony Brook, 255 Earth and Space Sciences Stony Brook, NY 11794-2100, USA. (adrogers@notes.cc.sunysb.edu)